Chemical Engineering Journal 503 (2025) 158442

Contents lists available at ScienceDirect

Chemical Engineering Journal

journal homepage: www.elsevier.com/locate/cej

Designed tumor microenvironment-remodeling bispolyphenol nanoparticles combined with αPD-L1 for enhanced melanoma immunotherapy

Yanzhu Wang [a,1], Linghe Zang [c,1], Liyuan Guan [a], Xihang Ren [a], Zongmin Xia [a], Zhou Li [d], Zhaoxu Meng [b,*], He Lian [b,*]

[a] Wuya College of Innovation, Shenyang Pharmaceutical University, Shenyang 110016, China
[b] Department of Biomedical Engineering, School of Medical Instrumentation, Shenyang Pharmaceutical University, Shenyang 110016, China
[c] Institute of Life Science and Bio-pharmaceuticals, Shenyang Pharmaceutical University, Shenyang 110016, China
[d] Beijing Institute of Nanoenergy and Nanosystems, Chinese Academy of Sciences, Beijing 101400, China

ARTICLE INFO

Keywords:
Glycolysis
Cuproptosis
Immunotherapy
Tumor microenvironment reprogramming
Bispolyphenol nanoparticles

ABSTRACT

The efficacy of αPD-L1, an immune checkpoint inhibitor, in the treatment of melanoma is limited by individual patient variations and tumor immunosuppressive cells. Consequently, current immunotherapy of melanoma is far from satisfactory. In this study, bispolyphenol nanoparticles (Phl-$CaCO_3$@Lut-Cu NPs) were constructed by wrapping a luteolin-copper (Lut-Cu) network around the surface of phloretin-loaded calcium carbonate (Phl-$CaCO_3$) nanoparticles. Upon entering tumor cells, Phl-$CaCO_3$@Lut-Cu nanoparticles efficiently released Cu^{2+}, phloretin (Phl), and luteolin (Lut) due to the acid-responsive properties of calcium carbonate and the metal-phenolic network. The copper ions mediated cuproptosis by binding to dihydrolipoamide acetyltransferase and induced cellular immune responses by promoting release of damage-associated molecular patterns (DAMPs). In addition, Phl blocked glucose transport by inhibiting glucose transporter 1 activity, thereby disrupting the energy supply process in tumor cells. Simultaneously, Lut inhibited expression of hypoxia-inducible factor-1α, negatively regulating aerobic glycolysis. This study aimed to reshape the tumor microenvironment by exploring the synergistic effects of cuproptosis and dual glycolysis inhibition, enhancing the T cell-mediated immune response, and suppressing tumor cell growth when combined with αPD-L1. This study provides a new perspective and strategy for melanoma immunotherapy.

1. Introduction

Melanoma is a malignant tumor that occurs in the skin, retina, and mucosal tissues, and is highly metastatic [1]. Traditional therapies have exhibited limited efficacy. Studies have indicated that melanoma is highly immunogenic, so immunotherapy could be a promising treatment option [2]. The immune checkpoint inhibitor αPD-L1 reverses the inactivation and depletion of T cells by specifically binding to the PD-L1 receptor on the surface of tumor cells, blocking its interaction with the PD-1 receptor on the surface of T cells, and restoring normal antitumor T cell activity [3,4]. However, in the case of melanoma immunotherapy, the positive response rate to immune checkpoint inhibitors alone is lower than anticipated, with the response to PD-1 monoclonal antibody being only around 30 % [5]. The poor performance is mainly attributed to individual differences in the expression levels of PD-L1, and the immune response to αPD-L1 is also affected by tumor immunosuppressive cells such as regulatory T cells (Treg), M2 macrophages, and myeloid-derived suppressor cells (MDSCs) [6–10]. Studies have shown that excess levels of copper can regulate the expression of PD-L1 on the surface of tumor cells, so the combination of copper and αPD-L1 is expected to reshape the immunosuppressive tumor microenvironment, enhancing the response of tumor cells to αPD-L1 and improving efficacy [11].

Under normal physiological conditions, ions such as Na^{+}, Ca^{2+}, Zn^{2+}, and Cu^{2+} play crucial roles in maintaining the dynamic balance of biological activities [12,13]. Of these ions, regulation of intracellular

* Corresponding authors.
E-mail addresses: mengzhaoxu2006@163.com (Z. Meng), lianhe126@126.com (H. Lian).
[1] These authors contributed equally to this work.

https://doi.org/10.1016/j.cej.2024.158442
Received 13 August 2024; Received in revised form 21 November 2024; Accepted 7 December 2024
Available online 9 December 2024

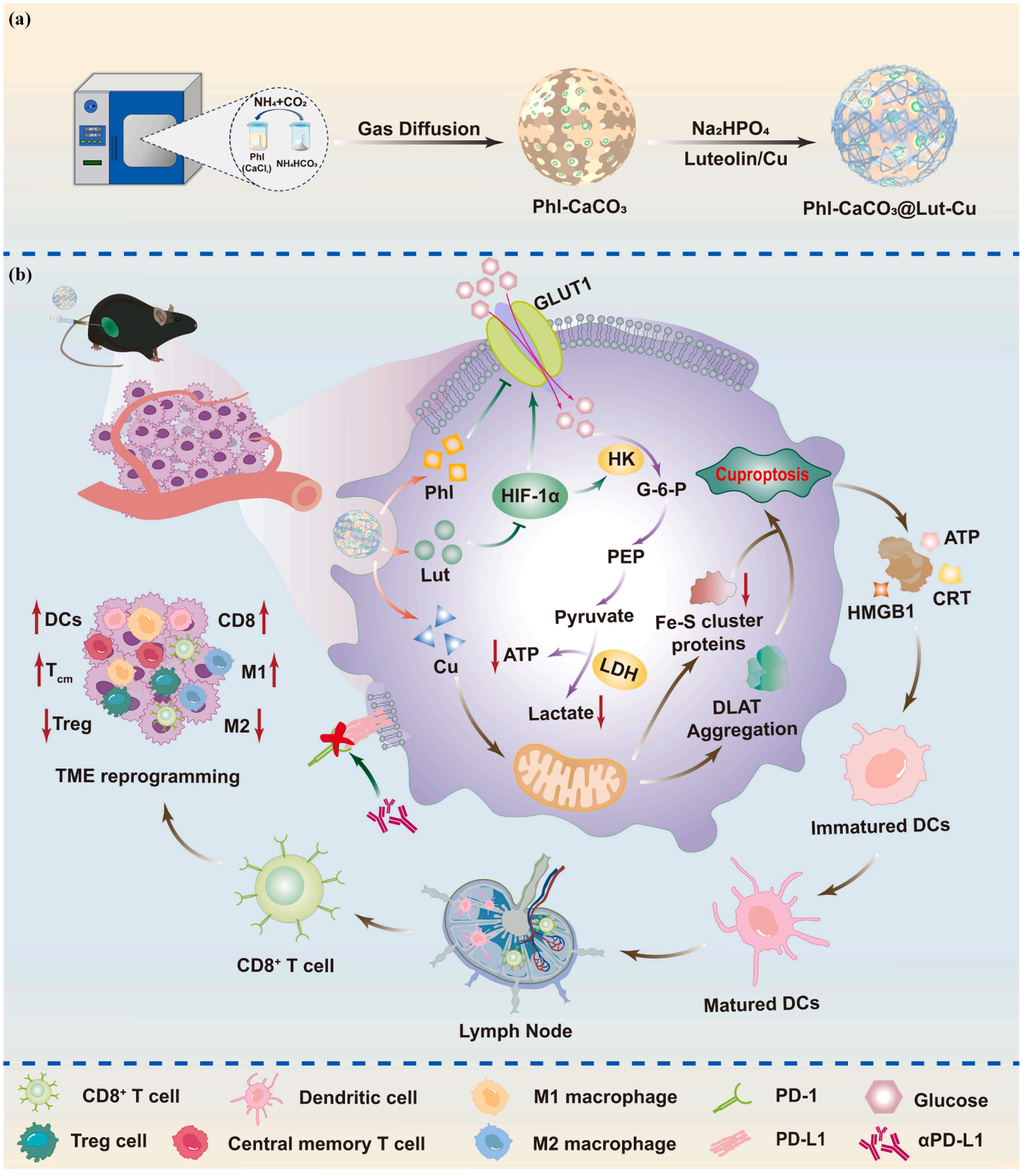

Fig. 1. Schematic illustration of the mechanism of Phl-$CaCO_3$@Lut-Cu combined with αPD-L1 for enhanced melanoma immunotherapy. (a) Preparation process of Phl-$CaCO_3$@Lut-Cu. (b) The biological mechanism of Phl-$CaCO_3$@Lut-Cu synergistically inhibits melanoma by dual regulation of glycolysis, cuproptosis, and immunosuppressive tumor microenvironment remodeling in combination with αPD-L1.

copper homeostasis is mediated by copper transporters, including SLC31A1 and ATP7B. However, ionic homeostasis can be disrupted in tumor cells through external regulation, thereby facilitating immunotherapy of tumors [14–19]. When there is an excess of intracellular copper ions, lipoylated proteins in the mitochondria aggregate, reducing the stability of Fe-S cluster proteins. This leads to a form of cell death that differs from apoptosis, cell necrosis, ferroptosis, and other cell death patterns, known as cuproptosis, which ultimately leads to the demise of tumor cells [20]. It has been reported that cuproptosis can promote the release of damage-associated molecular patterns (DAMPs), upregulate

extracellular ATP, induce migration of high mobility group protein B1 (HMGB1) from the nucleus to the extracellular space, and enhance calreticulin (CRT) expression on the surface of tumor cells [21]. This process ultimately promotes dendritic cell (DC) maturation and T cell activation, thereby initiating immune responses.

Unlike normal cells, which primarily generate energy for their physiological activities through mitochondrial oxidative phosphorylation, tumor cells in solid tumors favor glycolysis as their metabolic pathway, even in the presence of oxygen [22–24]. Tumor cells take-up glucose from the extracellular environment via glucose transporter 1 (GLUT1), perform aerobic glycolysis, and efficiently generate lactate and ATP to meet their energy requirements. The produced lactate is excreted, promoting formation of an immunosuppressive tumor microenvironment [25–29]. Therefore, the inhibition of glycolysis is beneficial for inhibiting tumor development and reshaping the tumor immune microenvironment. Phloretin (Phl), a dihydrochalcone flavonoid found in apples, is an effective inhibitor of GLUT1 [30–32]. It achieves "starvation treatment" by significantly inhibiting GLUT1 activity, thereby reducing glucose uptake and ultimately blocking the energy supply of tumor cells at the source. In addition, luteolin (Lut), a natural flavonoid compound, has been found to inhibit expression of hypoxia-inducible factor-1α (HIF-1α) to regulate the activity of key glycolytic proteins (such as GLUT1) [33–36]. Inhibition of the glycolytic process by Lut was confirmed in this study. The combination of Phl and Lut can therefore improve metabolic reprogramming by inhibiting glycolysis and reducing lactate production through dual site inhibition.

Inspired by the above mechanism, we designed biodegradable and tumor-responsive bispolyphenol $CaCO_3$ nanoparticles through the principle of gas diffusion and metal-phenolic network. Specifically, a luteolin-copper (Lut-Cu) metal-phenolic network was coated on the surface of phloretin-calcium carbonate (Phl-$CaCO_3$) nanoparticles, referred to as Phl-$CaCO_3$@Lut-Cu nanoparticles (Fig. 1). After Phl-$CaCO_3$@Lut-Cu enters tumor cells, Phl inhibits the activity of GLUT1, which in turn hinders the uptake of glucose and disrupts the glycolytic process, ultimately cutting-off the energy supply to tumor cells. Lut, released by dissociation of the Lut-Cu phenolic network under weakly acidic conditions, downregulates cyclin B1 and modulates the activity of glycolysis-related proteins by reducing expression of HIF-1α, thereby downregulating glycolysis. Phl and Lut regulate glycolysis through different mechanisms, leading to a significant reduction in the production of lactate and ATP, and improving the immunosuppressive tumor microenvironment. Furthermore, copper ions trigger cuproptosis and the release of DAMPs to initiate an immune response. The Phl-$CaCO_3$@Lut-Cu nanoparticles not only inhibit cell proliferation, but also enhance DC maturation and induce transformation of macrophages from M2 to M1 type. In addition, combination of the nanoparticles with αPD-L1 significantly promotes infiltration of $CD8^+$ T cells, reshaping the immunosuppressive tumor microenvironment, boosts T cell-mediated immune responses, and strongly induces tumor cell death. To the best of our knowledge, this is the first report of dual glycolytic inhibition-cuproptosis using bispolyphenols to enhance the efficacy of antitumor immunotherapy. The present nanosystem exhibited a potent synergistic effect and offers a new treatment concept for the future.

2. Materials and methods

2.1. Materials

Dopamine hydrochloride ($C_8H_{11}NO_2$•HCl) was purchased from Aladdin Biochemical Technology Co., Ltd, (Shanghai, China). Anhydrous calcium chloride ($CaCl_2$) and copper acetate monohydrate ($C_4H_6CuO_4{\cdot}H_2O$) were bought from Damao Chemical Reagent Factory (Tianjin, China). Phloretin (Phl), luteolin (Lut), ammonium bicarbonate (NH_4HCO_3), disodium hydrogen phosphate dodecahydrate ($Na_2HPO_4{\cdot}12H_2O$), and ethylenediaminetetraacetic acid disodium salt (EDTA•2Na) were obtained from Titan Scientific Co., Ltd. (Shanghai, China). Tris, RPMI 1640 medium, fetal bovine serum (FBS), BCA protein assay kit, CCK-8 assay kit, annexin V-fluorescein isothiocyanate (FITC)/propidium iodide (PI) apoptosis detection kit, and calcein AM/PI cell viability assay kit were purchased from Meilun Biotechnology Co. (Dalian, China). The cell cycle and apoptosis analysis kit, glucose assay kit, and ATP assay kit were purchased from Beyotime Biotechnology Co. (Haimen, China). The primary antibodies anti-CD3-FITC, anti-CD4-Percp-cy5.5, anti-CD8-APC, anti-CD25-BV421, anti-CD80-APC, anti-CD86-PE, anti-CD206-PE, anti-CD11b-FITC, anti-CD11c-BV421, anti-F4/80-APC, and anti-FOXP3-PE were all bought from BioLegend, Co., Ltd. (Beijing, China). The lactic acid assay kit was obtained from Elabscience Biotechnology Co. (Wuhan, China).

2.2. Synthesis of Phl-$CaCO_3$ nanoparticles

Phl-$CaCO_3$ nanoparticles were fabricated using a gas diffusion reaction according to a previous report [37]. $CaCl_2$ (150 mg), Phl (10 mg), and dopamine hydrochloride (2 mg) were dispersed in anhydrous ethanol (50 mL) using water bath ultrasonication. The mouth of the bottle was covered with tin foil, the foil was perforated, and the bottle placed in a vacuum drying oven with a beaker containing NH_4HCO_3 (5 g). The oven was then heated at 40 °C for 24 h. Finally, the resulting product was collected by centrifugation (8000 rpm, 15 min) and then freeze-dried.

2.3. Preparation and characterization of Phl-$CaCO_3$@Lut-Cu nanoparticles

Phl-$CaCO_3$ (10 mg) was dispersed in water (8 mL) and the pH was adjusted to alkaline by addition of sodium diphosphate solution (0.06 M, 2 mL). The mixture was homogeneously dispersed by water bath ultrasonication. Anhydrous ethanol solutions of Lut (5 mg/mL, 1 mL) and copper acetate (5 mg/mL, 1 mL) were added dropwise and the mixture stirred vigorously for 5 min. The Phl-$CaCO_3$@Lut-Cu nanoparticles were then collected by centrifugation (8000 rpm, 15 min), washed twice with deionized water, and then freeze-dried.

The morphology of the Phl-$CaCO_3$@Lut-Cu nanoparticles was characterized using a transmission electron microscope (TEM, Tecnai G20, FEI, USA). The crystal structure was observed using X-ray diffraction (XRD). The dynamic light scattering (DLS) size distribution and zeta potential of $CaCO_3$, Phl-$CaCO_3$, and Phl-$CaCO_3$@Lut-Cu were measured using a Malvern Zetasizer Nano series instrument (Malvern, UK). The thermogravimetric data were obtained using a thermogravimetric analyzer (DSC8231, RigaKu, Japan). The elemental composition was determined by X-ray photoelectron spectroscopy (XPS, ESCAlab250, Thermo Fisher Scientific, USA). To determine the drug loading efficiency of Phl-$CaCO_3$@Lut-Cu nanoparticles, two drops of concentrated hydrochloric acid were added to the nanoparticles (1 mg) for digestion. Subsequently, absolute ethanol (1 mL) was added and the absorbance values at 286 and 350 nm were measured using a UV–Vis spectrophotometer. Finally, the loading efficiencies of Phl and Lut were calculated based on the standard curve. To evaluate stability, the prepared Phl-$CaCO_3$@Lut-Cu was dispersed in different media, including phosphate-buffered saline (PBS) and serum, and stored at room temperature for various times. The particle size was then measured using the Malvern zetasizer.

2.4. In vitro drug release

Phl-$CaCO_3$@Lut-Cu solution (5 mL) was placed in a dialysis bag and shaken at 37 °C in PBS (30 mL) at pH 5.5, 6.5, or 7.4. Samples of dialysate were taken at 0, 2, 4, 6, 8, 10, and 12 h. The release profiles of Phl and Lut were determined by UV–Vis spectrophotometry, while the release of copper ions was determined by inductively coupled plasma-optical emission spectroscopy (ICP-OES).

2.5. Cell lines

The murine melanoma cell line (B16) was obtained from the Cell Bank of the Chinese Academy of Sciences (Shanghai, China) and was cultured in RPMI 1640 medium containing 10 % FBS and 1 % penicillin–streptomycin at 37 ℃ under 5 % CO_2.

2.6. Cellular uptake

B16 cells were seeded into a 12-well plate at a density of 1×10^5 cells/mL and incubated at 37 °C for 24 h. FITC-labeled Phl-$CaCO_3$@Lut-Cu (60 μg/mL, 100 μL) was added and incubated for 2, 4, or 6 h. The cells were then washed twice with PBS and labeled with Actin-Tracker Red-555. Subsequently, the nuclei were stained using Hoechst 33342 (1 μg/mL). Finally, fluorescence images were taken using a confocal laser scanning microscope (CLSM).

To determine lysosome escape, B16 cells were seeded into a 12-well plate at a density of 1×10^5 cells/mL and incubated at 37 °C for 24 h. FITC-labeled Phl-$CaCO_3$@Lut-Cu (60 μg/mL, 100 μL) was added and incubated for 2, 4, or 6 h. The cells were then washed twice with PBS and labeled with LysoTracker Red (60 nM) for 1 h. Subsequently, the cells were washed twice with PBS and the nuclei were stained using Hoechst 33342 (1 μg/mL) for 30 min. Finally, fluorescence images were taken using a CLSM.

2.7. In vitro cytotoxicity and cuproptosis evaluation

The cytotoxicity of Phl, $CaCO_3$, Phl-$CaCO_3$, Lut, $CaCO_3$@Lut-Cu, and Phl-$CaCO_3$@Lut-Cu towards B16 cells was determined using a CCK-8 assay kit. B16 cells were seeded into 96-well plates (3×10^4 cells/mL) and cultured for 24 h. The cells were then treated with different formulations at gradient concentrations (50, 100, 150, 200, and 250 μg/mL) for 12 h. Untreated cells served as the control group. Cell viability was measured using a CCK-8 assay kit.

For the cuproptosis assay, B16 cells were seeded into 96-well plates (3×10^4 cells/mL) and cultured for 24 h. The cells were then treated with different formulations ($CaCO_3$, Phl-$CaCO_3$, $CaCO_3$@Lut-Cu, Phl-$CaCO_3$@Lut-Cu) with or without tetrathiomolybdate (TTM, a copper ion chelator) for 12 h. Untreated cells served as the control group. Cell viability was measured using a CCK-8 assay kit.

2.8. Apoptosis and cell cycle assay

B16 cells were incubated in a 12-well plate (1×10^5 cells/mL) for 24 h and then incubated with Phl, $CaCO_3$, Phl-$CaCO_3$, Lut, $CaCO_3$@Lut-Cu, or Phl-$CaCO_3$@Lut-Cu for an additional 24 h. Subsequently, the cells were collected, washed with PBS, and resuspended in the binding buffer (100 μL). For the apoptosis assay, annexin V-FITC (8 μL) and PI (8 μL) were added to stain the cells for 15 min. For cell cycle assays, cells were collected and washed once with pre-cooled PBS, fixed with pre-chilled 70 % ethanol, and incubated with PI for 30 min at 37 ℃. After staining and incubation, the samples were analyzed using flow cytometry (BD LSRFortessa X-20, USA).

2.9. Live/dead cell staining

B16 cells were seeded into a 12-well plate and incubated at 37 ℃ for 24 h. The cells were then treated with Phl, $CaCO_3$, Phl-$CaCO_3$, Lut, $CaCO_3$@Lut-Cu, or Phl-$CaCO_3$@Lut-Cu (80 μg/mL) for 12 h. Subsequently, the B16 cells were stained with calcein AM/PI in the dark for 30 min. Cells were observed using a fluorescence microscope (MS60-2, China).

2.10. Cuproptosis and glycolysis pathway evaluation

B16 cells were incubated in a 6-well plate for 24 h and then treated with Phl, $CaCO_3$, Phl-$CaCO_3$, Lut, $CaCO_3$@Lut-Cu, or Phl-$CaCO_3$@Lut-Cu at varying concentrations for 12 h. Lactate levels were assessed using a lactic acid colorimetric assay kit and the glucose concentration was determined using a glucose assay kit with O-toluidine. Additionally, ATP content was determined using an ATP assay kit, and the intracellular Cu concentration was determined using a cell copper colorimetric assay kit. Protein concentrations in the aforementioned samples were quantified using a BCA protein assay kit.

To assess the impact of nanosystem on mitochondrial damage, B16 cells were incubated in a 12-well plate at a density of 1×10^5 cells/mL for 24 h. Subsequently, the cells were treated with $CaCO_3$, Phl-$CaCO_3$, $CaCO_3$@Lut-Cu, or Phl-$CaCO_3$@Lut-Cu for an additional 12 h. Following treatment, rhodamine 123 was used as a probe to detect mitochondrial membrane potential. Additionally, cells were stained with Hoechst 33342 to identify their location. To further investigate the effects of Phl-$CaCO_3$@Lut-Cu on mitochondria, we employed bio-transmission electron microscopy (bio-TEM) to examine the mitochondrial morphology of cells treated with Phl-$CaCO_3$@Lut-Cu.

2.11. Immunofluorescence assay

To evaluate the effect of Phl-$CaCO_3$@Lut-Cu on immune responses, B16 cells were seeded into a 12-well plate and incubated for 24 h at 37 °C. Subsequently, the cells were treated with Phl, $CaCO_3$, Phl-$CaCO_3$, Lut, $CaCO_3$@Lut-Cu, or Phl-$CaCO_3$@Lut-Cu (60 μg/mL) for 12 h. The cells were incubated with primary and fluorescent secondary antibodies, and then the cell nuclei were stained with 4′,6-diamidino-2-phenylindole (DAPI). Finally, all samples were examined by CLSM.

2.12. Western blot

B16 cells were seeded into 6-well plates and incubated at 37 ℃ for 24 h. The cells were then treated with Phl, $CaCO_3$, Phl-$CaCO_3$, Lut, $CaCO_3$@Lut-Cu, or Phl-$CaCO_3$@Lut-Cu (60 μg/mL) for 5 h and the cells harvested to extract proteins following the manufacturer's procedures. The extracted proteins were separated by sodium dodecyl sulfate–polyacrylamide gel electrophoresis (SDS-PAGE) and transferred to polyvinylidene fluoride (PVDF) membranes. Subsequently, the PVDF membranes were blocked with 5 % skim milk and then incubated with primary and secondary antibodies. Finally, the protein bands were exposed and quantified using ImageJ software.

2.13. Animal and tumor models

All animal experiments were approved by the Animal Research Committee of Shenyang Pharmaceutical University. The C57BL/6 mice were purchased from Changsheng Biotechnology Co. Ltd (Benxi, China). The xenograft B16 tumor models were established in female C57BL/6 mice by subcutaneous injection of B16 cells.

2.14. In vivo biocompatibility analysis

Healthy Kunming mice were randomly divided into seven groups and subcutaneously injected with saline (control group), Phl, $CaCO_3$, Phl-$CaCO_3$, Lut, $CaCO_3$@Lut-Cu, or Phl-$CaCO_3$@Lut-Cu (10 mg/kg). The mice were sacrificed after 12 days. Blood samples were collected for hematological and biochemical analysis and the main organs were collected for hematoxylin and eosin (H&E) staining.

2.15. Evaluation of in vivo antitumor efficacy

When the tumor volume reached approximately 100 mm^3, the B16 tumor-bearing mice were randomly divided into seven groups. Mice in each group were subjected to intratumoral injection of saline (control group), Phl, $CaCO_3$, Phl-$CaCO_3$, Lut, $CaCO_3$@Lut-Cu, or Phl-$CaCO_3$@-Lut-Cu (10 mg/kg) on days 0, 4, and 8. Body weights and tumor

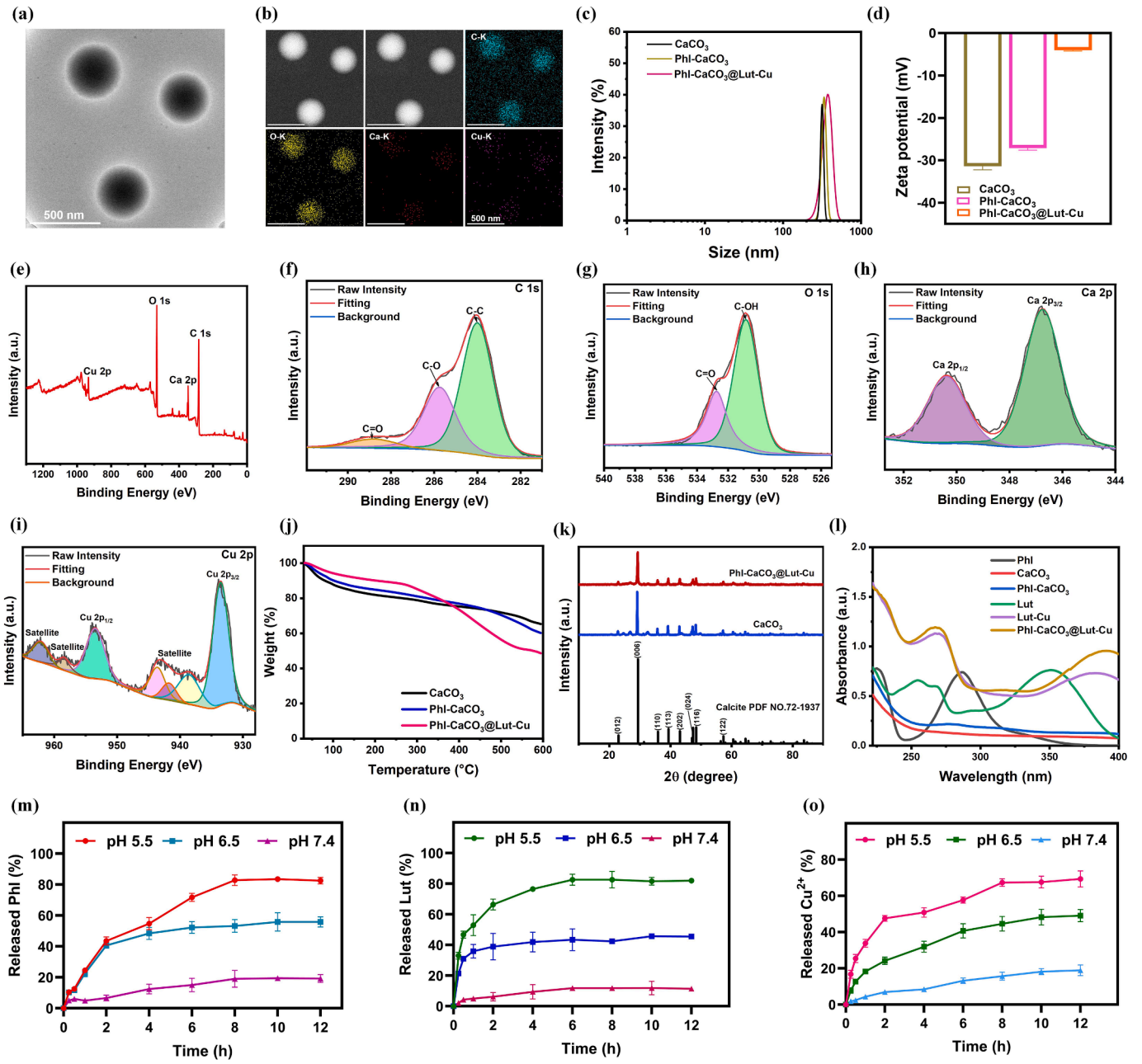

Fig. 2. Characterization of Phl-$CaCO_3$@Lut-Cu. (a) Representative TEM images of Phl-$CaCO_3$@Lut-Cu. (b) Element mapping of Phl-$CaCO_3$@Lut-Cu. Particle size distribution (c) and zeta potentials (d) of $CaCO_3$, Phl-$CaCO_3$ and Phl-$CaCO_3$@Lut-Cu by DLS analysis. (e) XPS analysis of Phl-$CaCO_3$@Lut-Cu. High-resolution C1s (f), O1s (g), Ca2p (h), and Cu2p (i) XPS spectra of Phl-$CaCO_3$@Lut-Cu. (j) TGA curves of $CaCO_3$, Phl-$CaCO_3$ and Phl-$CaCO_3$@Lut-Cu. (k) XRD analysis of $CaCO_3$ and Phl-$CaCO_3$@Lut-Cu. (l) UV–Vis spectra of Phl, $CaCO_3$, Phl-$CaCO_3$, Lut, Lut-Cu and Phl-$CaCO_3$@Lut-Cu. The release profiles of phloretin (m), luteolin (n), and Cu^{2+} (o) from Phl-$CaCO_3$@Lut-Cu at different pH values.

volumes were measured on alternate days. After completion of treatment, the tumors in each group were collected from the sacrificed mice for H&E, Ki67, dihydrolipoamide acetyltransferase (DLAT), GLUT1, and HIF-1α immunohistochemical staining assays, and TdT-mediated dUTP nick-end labeling (TUNEL), HMGB1, CRT, CD4, and CD8 immunofluorescence analysis. Additionally, tumor homogenate supernatants were collected to determine cytokine levels by enzyme-linked immunosorbent assay (ELISA). Furthermore, the tumors were digested to produce single-cell suspensions to analyze the frequency of $CD4^+$ T cells, $CD8^+$ T cells, Treg cells, M1 and M2 macrophages, and mature DCs using flow cytometry.

2.16. In vivo immune antitumor effect of Phl-$CaCO_3$@Lut-Cu combined with αPD-L1

Subcutaneous B16 bilateral tumor models were established in C57BL/6 mice. B16 cells (1×10^6 cells/mouse) were subcutaneously injected into the right and left flanks of each mouse as the primary and distal tumors on day − 7 and day 0, respectively. When the primary tumor volume reached approximately 100 mm^3, the xenograft B16 tumor mice were randomly assigned into four groups followed by intratumoral injection of saline (control group), αPD-L1 (1 mg/kg), Phl-$CaCO_3$@Lut-Cu (10 mg/kg), and Phl-$CaCO_3$@Lut-Cu + αPD-L1, respectively. Body weights and tumor volumes were measured every other day. Finally, the mice were sacrificed, and the tumors, lymph

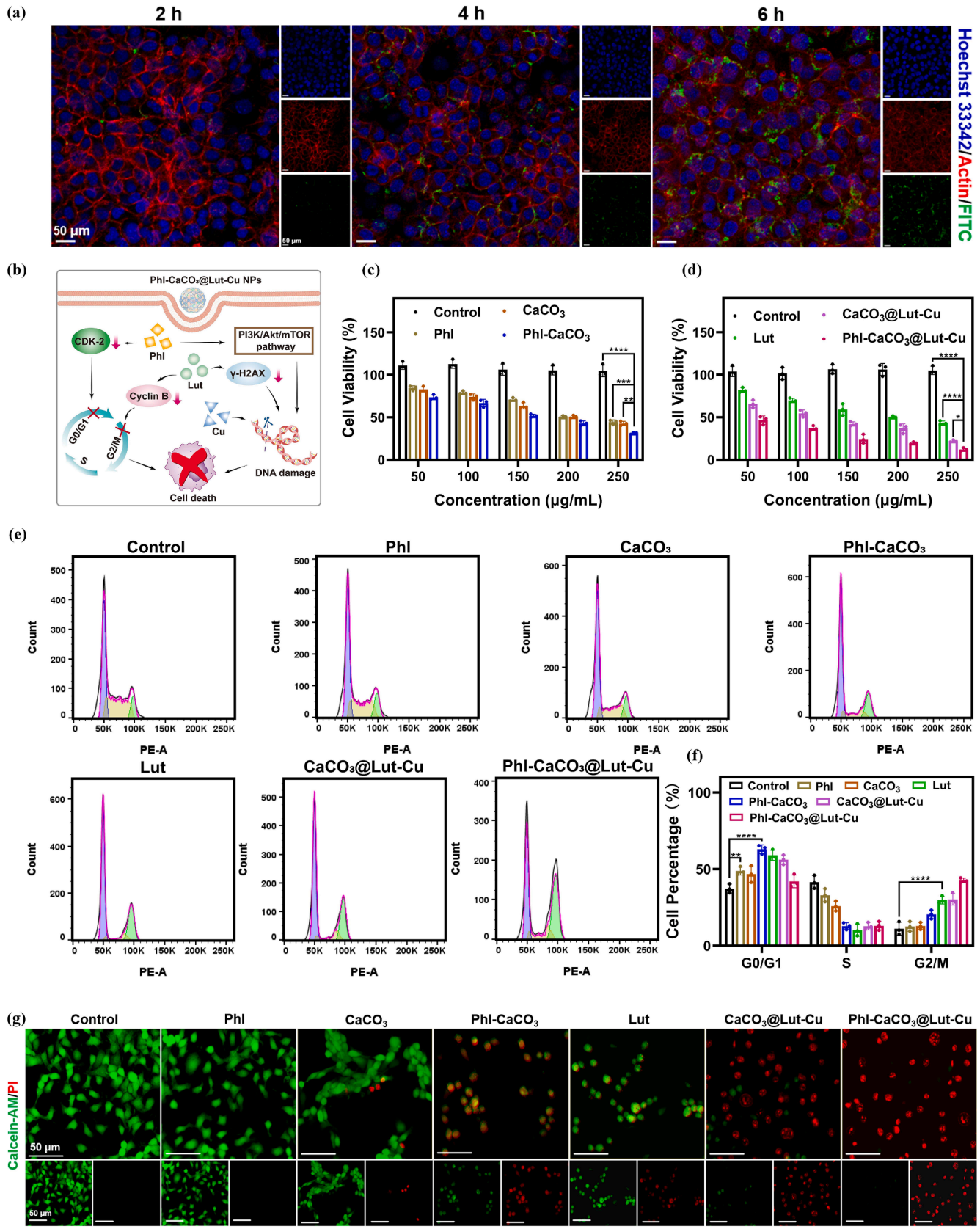

Fig. 3. *In vitro* antitumor activity of Phl-$CaCO_3$@Lut-Cu. (a) The cellular uptake behavior of B16 cells after incubation with FITC labeled Phl-$CaCO_3$@Lut-Cu for 2 h, 4 h, 6 h, respectively. (b) The mechanism of cell death induced by Phl-$CaCO_3$@Lut-Cu NPs. (c, d) The viability of B16 tumor cells in various treatment groups. Representative flow cytometry profiles (e) and semi-quantification (f) of the cell cycle distribution of B16 cells after various treatments. (g) The fluorescent images of B16 cells with different treatments, stained with calcein-AM (green, live cells) and PI (red, dead cells), respectively. ($n = 3$, $^{*}P < 0.05$, $^{**}P < 0.01$, $^{***}P < 0.001$, $^{****}P < 0.0001$). (For interpretation of the references to colour in this figure legend, the reader is referred to the web version of this article.)

nodes, and spleens were collected for analysis of $CD4^+$ T cells, $CD8^+$ T cells, Treg cells, central memory (T_{cm}) cells, M1 and M2 macrophages, and mature DCs using flow cytometry. The intratumoral levels of TNF-α, IL-6, IL-12P70, and IFN-γ were measured using ELISA kits according to the manufacturer's protocols.

2.17. Statistical analysis

All data were processed with Origin, GraphPad Prism and ImageJ software. Quantitative data are presented as mean ± SD. One-way or two-way statistical analysis was performed when multiple groups were compared. P values less than 0.05 indicate a significant difference. $^{*}P < 0.05$, $^{**}P < 0.01$, $^{***}P < 0.001$, $^{****}P < 0.0001$.

3. Results

3.1. Preparation and characterization of Phl-$CaCO_3$@Lut-Cu

The Phl-$CaCO_3$@Lut-Cu nanoparticles were prepared by gas diffusion and chemical coordination. Simply, Phl, $CaCl_2$, and dopamine hydrochloride were first dissolved in ethanol and then the mixed solution was reacted with the gas generator, NH_4HCO_3, in a vacuum environment to form spherical Phl-$CaCO_3$ nanoparticles. Subsequently, a Lut-Cu^{2+} metal-polyphenol network was coated onto the surface of the Phl-$CaCO_3$ nanoparticles in a one-pot method to obtain Phl-$CaCO_3$@Lut-Cu nanoparticles (Fig. 1a). The average drug loading efficiencies of Phl, Lut, and Cu^{2+} in Phl-$CaCO_3$@Lut-Cu nanoparticles were calculated to be 10.03 %, 30.02 %, and 8.77 %, respectively, as determined by UV–Vis spectrophotometry and ICP-OES. The morphology of the nanoparticles was characterized by TEM. As shown in Fig. 2a, the nanoparticles had spherical structures and exhibited good dispersion in aqueous solution, which is consistent with the DLS result of 370 nm (Fig. 2c). In addition, the hydrodynamic diameters of $CaCO_3$, Phl-$CaCO_3$, and Phl-$CaCO_3$@-Lut-Cu nanoparticles increased progressively, illustrating the loading of Phl and the formation of a metal-polyphenol network. The zeta potentials of $CaCO_3$, Phl-$CaCO_3$, and Phl-$CaCO_3$@Lut-Cu nanoparticles were −31.43, −27.17, and −4.08 eV, respectively (Fig. 2d). This may be attributed to the charge neutralization that occurs between Cu^{2+} and Phl-$CaCO_3$. We also assessed the changes in particle size of Phl-$CaCO_3$@Lut-Cu nanoparticles in various environments by DLS. The results (Fig. S1) indicated that Phl-$CaCO_3$@Lut-Cu nanoparticles remained stable for 48 h in both PBS and serum, demonstrating their good stability.

The elemental mapping results showed that Phl-$CaCO_3$@Lut-Cu nanoparticles contained C, O, Ca and Cu elements, and the signals were uniformly distributed (Fig. 2b). The presence of C, O, Ca, and Cu was confirmed by XPS (Fig. 2e). As shown in Fig. 2f–i, the high-resolution C1s fitting results showed three characteristic peaks: 283.98, 285.78, and 288.88 eV, corresponding to C—C, C—O, and C═O groups, respectively. The two characteristic peaks on the O1s fitting curves at 530.88 and 532.78 eV corresponded to C—OH and C═O groups, respectively. The Ca in $CaCO_3$ was also clearly observed. In addition, the high-resolution Cu 2p analysis showed peak binding energies of 953.48 and 933.38 eV corresponding to Cu2p1/2 and Cu2p3/2, respectively.

Compared with 34.64 % weight loss of $CaCO_3$ nanoparticles, the weight losses of Phl-$CaCO_3$ and Phl-$CaCO_3$@Lut-Cu were 39.76 %, and 51.32 %, respectively (Fig. 2j). The increased weight loss indicated successful loading of Phl and effective coating by the Lut-Cu network. The crystal forms of $CaCO_3$ and Phl-$CaCO_3$@Lut-Cu were characterized by powder XRD. As shown in Fig. 2k, peaks in the spectrum of $CaCO_3$ were consistent with those of calcite $CaCO_3$, and peaks in the spectrum of Phl-$CaCO_3$@Lut-Cu nanoparticles were similar. To further demonstrate the successful preparation of Phl-$CaCO_3$@Lut-Cu, UV–Vis absorption spectroscopy was performed (Fig. 2l). Phloretin gave rise to a maximum absorption peak at 286 nm, while there were no distinct absorption peaks for $CaCO_3$. The degree of conjugation in the system decreased after formation of Phl-$CaCO_3$. Consequently, the peak at 286 nm was blue-shifted and the absorption intensity decreased significantly, indicating successful synthesis of Phl-$CaCO_3$. The maximum absorption peaks in the spectrum of Lut alone were located at 254 and 351 nm. After coordination with Cu^{2+}, the absorption peaks shifted towards longer wavelengths, which was attributed to the enhanced conjugation effect between Lut and Cu^{2+}. After assembling into Phl-$CaCO_3$@Lut-Cu, the peak at 254 nm was blue-shifted due to the electron-deficient Lut-Cu system.

3.2. In vitro drug release

To evaluate acid-responsive release, a Phl-$CaCO_3$@Lut-Cu solution was immersed in PBS at pH 5.5, 6.5, or 7.4 (Fig. 2m–o). The results showed that the Phl-$CaCO_3$@Lut-Cu solution exhibited better release performance under acidic conditions (pH 5.5) compared with pH 6.5 or 7.4. As expected, there was similar acid-responsive release of Phl, Lut, and Cu^{2+} ions, with cumulative release percentages of 82.51 %, 81.99 %, and 69.31 %, respectively at pH 5.5. This phenomenon was mainly attributed to the acid-responsive properties of $CaCO_3$ and the coordination bonds of the metal-polyphenol network. This property allowed Phl-$CaCO_3$@Lut-Cu to effectively release therapeutic components in the acidic environment of the tumor.

3.3. Cellular uptake of Phl-$CaCO_3$@Lut-Cu

To evaluate cellular uptake of FITC-labeled Phl-$CaCO_3$@Lut-Cu nanoparticles, images of the nanoparticles entering B16 melanoma cells were captured by CLSM (Fig. 3a). After 2 h incubation of FITC-labeled Phl-$CaCO_3$@Lut-Cu with B16 cells, only a faint green fluorescence was observed in the cells, suggesting incomplete entry of the nanoparticles at that time. After 4 h incubation with B16 cells, the green fluorescence within the cells became more pronounced, and further intensified after 6 h incubation. The results indicated that Phl-$CaCO_3$@Lut-Cu nanoparticles were effectively taken up by B16 cells. This uptake could potentially enhance therapeutic efficacy toward tumors and mitigate against non-specific uptake at non-tumor sites associated with the administration of Phl-$CaCO_3$@Lut-Cu nanoparticles. Importantly, Phl-$CaCO_3$@Lut-Cu nanoparticles have lysosomal escape capabilities that enable them to traverse the cell membrane and release drugs into the cytoplasm. As shown in Fig. S2, after 2 h incubation with the cells, a significant amount of red fluorescence and only weak green fluorescence were observed. This indicates that the Phl-$CaCO_3$@Lut-Cu nanoparticles had not fully entered the cells, and that the lysosomes remained relatively intact. In contrast, after 6 h incubation, more distinct separation of green and red fluorescence was observed, suggesting that the colocalization of Phl-$CaCO_3$@Lut-Cu nanoparticles and lysosomes was significantly reduced. These results demonstrate that Phl-$CaCO_3$@Lut-Cu nanoparticles effectively escaped from lysosomes. This phenomenon may be attributed to the "proton sponge effect" generated by the metal-phenolic network (MPN) [38], which disrupts the lysosomal membrane and ultimately facilitates escape of Phl-$CaCO_3$@Lut-Cu nanoparticles from lysosomes, leading to the release of phloretin, luteolin, and copper.

3.4. In vitro antitumor activity of Phl-$CaCO_3$@Lut-Cu

3.4.1. Evaluation of Phl-$CaCO_3$@Lut-Cu-mediated cell death

The *in vitro* effects of various formulations on B16 cells were assessed using a CCK-8 assay kit. Phl-$CaCO_3$ exhibited higher cytotoxicity than Phl or $CaCO_3$ alone, possibly due to the combined effect of glycolysis inhibition by Phl and mitochondrial apoptosis caused by overload of Ca^{2+} ions (Fig. 3c). Due to cuproptosis induced by Cu^{2+} and glycolysis inhibition by Lut, $CaCO_3$@Lut-Cu exhibited stronger cytotoxicity. As expected, Phl-$CaCO_3$@Lut-Cu exhibited the strongest cytotoxicity due to the synergistic effects of cuproptosis and dual glycolysis inhibition (Fig. 3d). The rates of cell death and IC_{50} values in each group were also

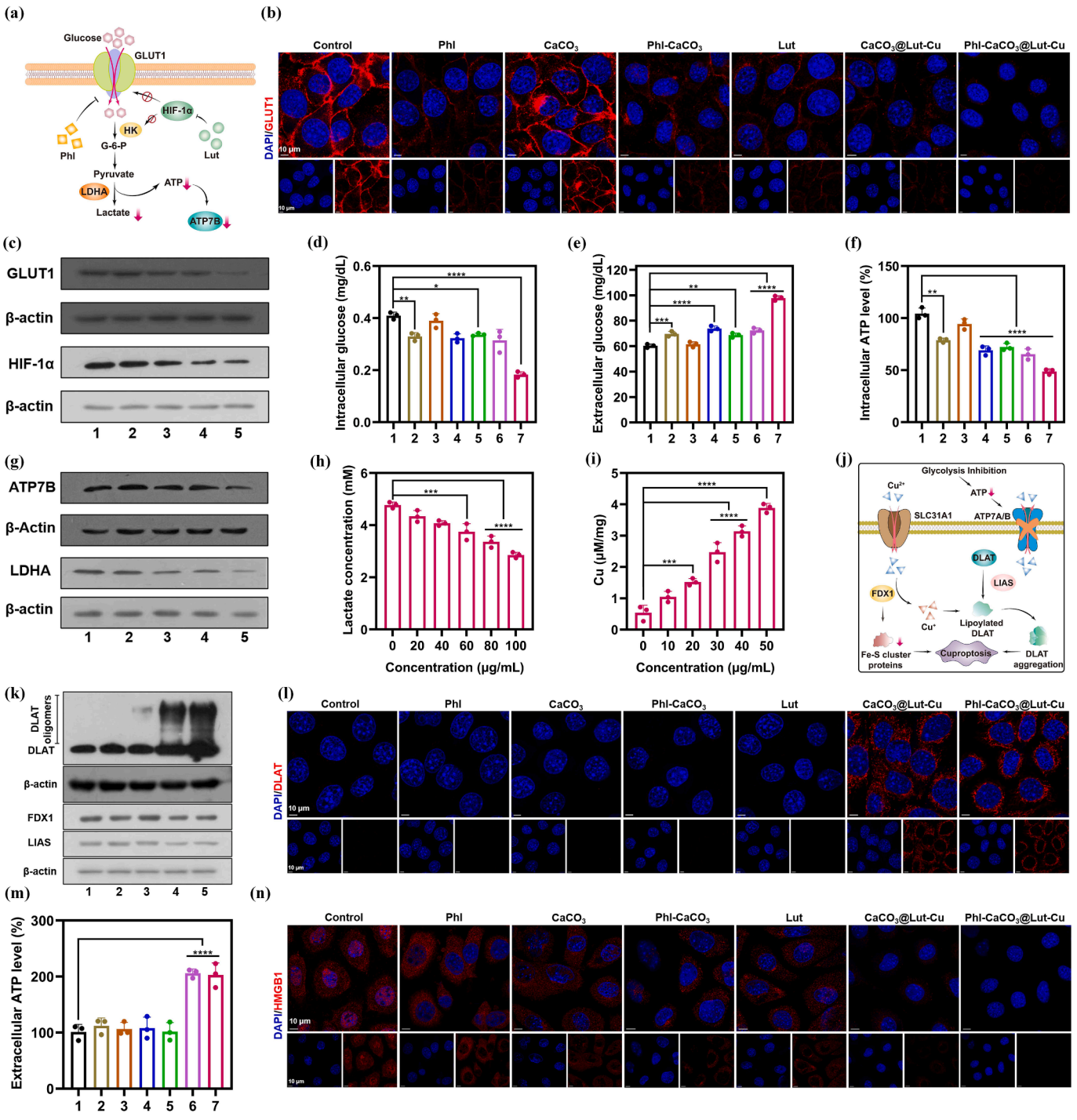

Fig. 4. Studies on the glycolysis inhibition and cuproptosis mediated by Phl-$CaCO_3$@Lut-Cu in vitro. (a) The glycolysis mechanism induced by Phl-$CaCO_3$@Lut-Cu. (b) Immunofluorescence images of GLUT1 in B16 cells after different treatments. (c) Western blotting analysis of GLUT1 and HIF-1α proteins with various treatments. Intracellular (d) and extracellular (e) glucose levels after various treatments. (f) Intracellular relative ATP levels after different treatments. (g) Western blotting analysis of ATP7B and LDHA proteins in B16 cells after various treatments. (h) Lactate levels in the supernatant of the cell culture medium with various treatments. (i) Intracellular copper contents after incubation with Phl-$CaCO_3$@Lut-Cu at different concentration. (j) The cuproptosis mechanism mediated by Phl-$CaCO_3$@Lut-Cu. (k) Western blotting analysis of cuproptosis-related proteins expression in B16 cells after various treatments. (l) Immunofluorescence images of DLAT oligomers in B16 cells with different treatments. (m) Extracellular relative ATP levels after different treatments. (n) Immunofluorescence images of HMGB1 in B16 cells after different treatments. (1:Control, 2:Phl, 3:$CaCO_3$, 4:Phl-$CaCO_3$, 5:Lut, 6:$CaCO_3$@Lut-Cu, 7:Phl-$CaCO_3$@Lut-Cu). (western blotting analysis:1:Control, 2:$CaCO_3$, 3:Phl-$CaCO_3$, 4:$CaCO_3$@Lut-Cu, 5:Phl-$CaCO_3$@Lut-Cu). (n = 3, *P < 0.05, **P < 0.01, ***P < 0.001, ****P < 0.0001).

calculated (Fig. S3).

3.4.2. Study of apoptosis and cell-cycle effects of Phl-$CaCO_3$@Lut-Cu

Apoptosis of B16 cells treated with different formulations was also assessed using flow cytometry (Fig. S4a and b). The results showed that incorporation of the Lut-Cu phenolic network was an important cause of apoptosis, with the apoptosis rate of 33.60 % in the $CaCO_3$@Lut-Cu group being approximately 3 times those of Phl, $CaCO_3$, or Lut groups. Notably, dual inhibition of glycolysis combined with the cuproptosis effect meant that Phl-$CaCO_3$@Lut-Cu exhibited the strongest

cytotoxicity, resulting in the highest apoptosis rate (48.87 %). These results collectively indicated that Phl-$CaCO_3$@Lut-Cu could have a potent antitumor effect.

Cellular proliferation is dependent on the cell cycle, so we also investigated the effects of different preparations on the cell cycle using flow cytometry. As presented in Fig. 3e and f, the number of cells in G0/G1 phase significantly increased in the Phl-treated group. This increase may be attributed to the induction of cell cycle arrest in G0/G1 phase by Phl, which may be associated with downregulated expression of cell-cycle proteins such as CDK-2, CDK-4, and cyclin-E, as reported in the literature [39]. The number of cells in G0/G1 phase was also significantly increased in the Phl-$CaCO_3$ group. Furthermore, consistent with the report that Lut can induce cell cycle arrest in G2/M phase by downregulating cyclin B [40], the number of cells in G2/M phase increased significantly after treatment with Lut, $CaCO_3$@Lut-Cu or Phl-$CaCO_3$@Lut-Cu. These results suggest that cell cycle arrest induced by Phl and Lut play a non-negligible role in the anti-tumor effect of Phl-$CaCO_3$@Lut-Cu.

3.4.3. Cellular fluorescence analysis

To further explore the *in vitro* cytotoxicity of Phl-$CaCO_3$@Lut-Cu, we conducted calcein-AM and PI staining to distinguish living and dead cells (Fig. 3g). Compared with the bright green fluorescence of the control and Phl groups, the $CaCO_3$ and Lut groups exhibited red fluorescence, suggesting that $CaCO_3$ and Lut had specific cytotoxic effects on tumor cells. Furthermore, the Phl-$CaCO_3$ group exhibited a degree of red fluorescence, attributed to the acid-responsive nature of $CaCO_3$ and specific delivery of Phl into B16 cells. A brighter red fluorescence signal was observed in the $CaCO_3$@Lut-Cu group, due to the combination of cuproptosis, cell cycle arrest and glycolysis inhibition. Specifically, the synergistic effects of cuproptosis and dual glycolysis inhibition led to tumor cells treated with Phl-$CaCO_3$@Lut-Cu emitting the brightest red fluorescence, indicating the most potent cytotoxicity.

To evaluate the effects of Phl-$CaCO_3$@Lut-Cu on DNA, a DNA damage detection kit (γ-H2AX immunofluorescence method) was used (Fig. S5). Studies have shown that Phl can induce DNA damage and apoptosis by activating p53, modulating the Bcl2/Bax ratio, and inhibiting the PI3K/Akt/mTOR pathway [41]. Compared with the control group, the Phl group exhibited a certain level of green fluorescence. As a consequence of the acid responsiveness of $CaCO_3$, Phl was more specifically released in tumor cells, resulting in stronger green fluorescence in the Phl-$CaCO_3$ group. Moreover, Lut can induce significant DNA damage and inhibit the survival and growth of tumor cells, while copper ions have also been found to bind to guanine and cytosine on the opposite strand of DNA, leading to DNA damage in a variety of biological systems [42–44]. Therefore, due to the combined effects of Lut and copper ions, the green fluorescence intensity in the $CaCO_3$@Lut-Cu group was significantly increased. The brightest green fluorescence was observed in the Phl-$CaCO_3$@Lut-Cu group, indicating that it induced more serious DNA damage to tumor cells due to the synergistic effects of Phl, Lut, and copper ions.

3.5. Mechanism of cell death caused by Phl-$CaCO_3$@Lut-Cu

3.5.1. Validation of dual glycolysis inhibition by Phl-$CaCO_3$@Lut-Cu

Tumor cells take-up glucose from the extracellular environment and undergo aerobic glycolysis, which eventually produces a large amount of lactic acid and ATP. These compounds provide energy for tumor cells to survive and grow. In this process, GLUT1 plays an important role as the main protein responsible for facilitating entry of glucose into cells. Therefore, we determined the expression of GLUT1 in tumor cells using western blot and immunofluorescence imaging methods (Figs. 4b, c and S6a). The results showed that, compared with the control and $CaCO_3$ groups, Phl effectively downregulated GLUT1 expression, which was reflected by the weakened protein bands and decreased red fluorescence in the Phl-$CaCO_3$ group. Studies have shown that HIF-1α can promote transcriptional regulation of GLUT1 and regulate glycolysis [45]. Therefore, due to the effective inhibition of HIF-1α and feedback downregulation of glucose uptake brought about by Lut, expression of GLUT1 protein in the $CaCO_3$@Lut-Cu group also significantly decreased. As expected, Phl-$CaCO_3$@Lut-Cu exhibited the most pronounced inhibition of GLUT1 expression, manifested in the weakest fluorescence and the least amount of protein expression. The band and semi-quantitative result for HIF-1α protein in each group are shown in Figs. 4c and S6b, indicating that Phl-$CaCO_3$@Lut-Cu undoubtedly broke the positive feedback between HIF-1α and glycolysis. Subsequently, intracellular and extracellular glucose levels were assessed with a glucose assay kit using O-toluidine (Fig. 4d and e). Compared with the control group, the intracellular glucose level was significantly reduced, and the extracellular glucose level was significantly increased in the Phl or Lut-containing treatment groups, particularly in the Phl-$CaCO_3$@Lut-Cu group. The intracellular ATP level showed a similar trend (Fig. 4f). The results showed that intracellular glucose and ATP levels decreased by approximately 44.74 % and 48.72 %, respectively, after treatment with Phl-$CaCO_3$@Lut-Cu. This was a consequence of dual glycolysis inhibition due to downregulated expression of GLUT1 and HIF-1α by Phl and Lut, respectively. Inhibition of aerobic glycolysis in tumor cells ultimately led to decreased lactate content (Fig. 4h). Furthermore, the western blot results indicated that expression of ATP7B and lactate dehydrogenase A (LDHA) were also significantly downregulated after Phl-$CaCO_3$@Lut-Cu treatment (Figs. 4g, S6c, and d).

3.5.2. Evaluation of cuproptosis mediated by Phl-$CaCO_3$@Lut-Cu

Cuproptosis is a novel mechanism of copper ion-dependent regulatory cell death. Ferredoxin 1 (FDX1) and lipoyl synthetase (LIAS) are upstream regulators of protein lipoylation. FDX1 can reduce Cu^{2+} to Cu^{+} and then bind to the lipoic acid esterification component DLAT in the mitochondrial tricarboxylic acid cycle with the help of LIAS. This process results in the loss of Fe-S cluster proteins and the oligomerization of lipoylated proteins, which, in turn, induces acute protein toxic stress and ultimately leads to tumor cell death. Therefore, the intracellular concentration of copper ions after Phl-$CaCO_3$@Lut-Cu treatment was first measured using a cellular copper colorimetric kit. As presented in Figs. 4i and S7a, the cellular copper ion content increased in a concentration- and time-dependent manner, reaching 3.89 μM/mg when the concentration of Phl-$CaCO_3$@Lut-Cu was 50 μg/mL. When cells were incubated with Phl-$CaCO_3$@Lut-Cu for 10 h, the intracellular copper ion content was 7.87 times higher than that of the control group. The results indicated that Phl-$CaCO_3$@Lut-Cu nanoparticles effectively increased the concentration of copper ions in cells. This may be because efficient endocytosis of Phl-$CaCO_3$@Lut-Cu allows a large amount of copper to enter the cell in the form of a metal-phenolic network. Meanwhile, Phl and Lut in the nanoparticle lead to down-regulated expression of ATP7B, a protein responsible for copper transfer, by inhibiting glycolysis and the production of ATP, since copper ion transport is an energy-dependent process. This change leads to an imbalance of intracellular copper ion homeostasis and the accumulation of copper ions in the cell.

To further illustrate the *in vitro* cytotoxicity due to cuproptosis in B16 cells, the effects of different formulations and concentration gradients of Phl-$CaCO_3$@Lut-Cu co-incubated with TTM on cell viability were evaluated using a CCK-8 assay kit. As shown in Fig. S7b and c, the viability of tumor cells increased to a certain extent after co-incubation with TTM and a gradient concentration of Phl-$CaCO_3$@Lut-Cu or different formulations, suggesting the occurrence of cuproptosis in tumor cells.

Lipoylation of DLAT is an important process during cuproptosis, in which Cu^{+} ions can bind to thioctyl-acylated DLAT, causing abnormal oligomerization of DLAT. Consequently, the expression of DLAT was assessed by western blotting. As illustrated in Figs. 4k and S7d, the copper-containing treatment groups ($CaCO_3$@Lut-Cu and Phl-$CaCO_3$@Lut-Cu) exhibited significantly greater DLAT oligomerization compared to the control, $CaCO_3$, and Phl-$CaCO_3$ treatment groups, and the expression of DLAT in these groups increased to approximately 1.69

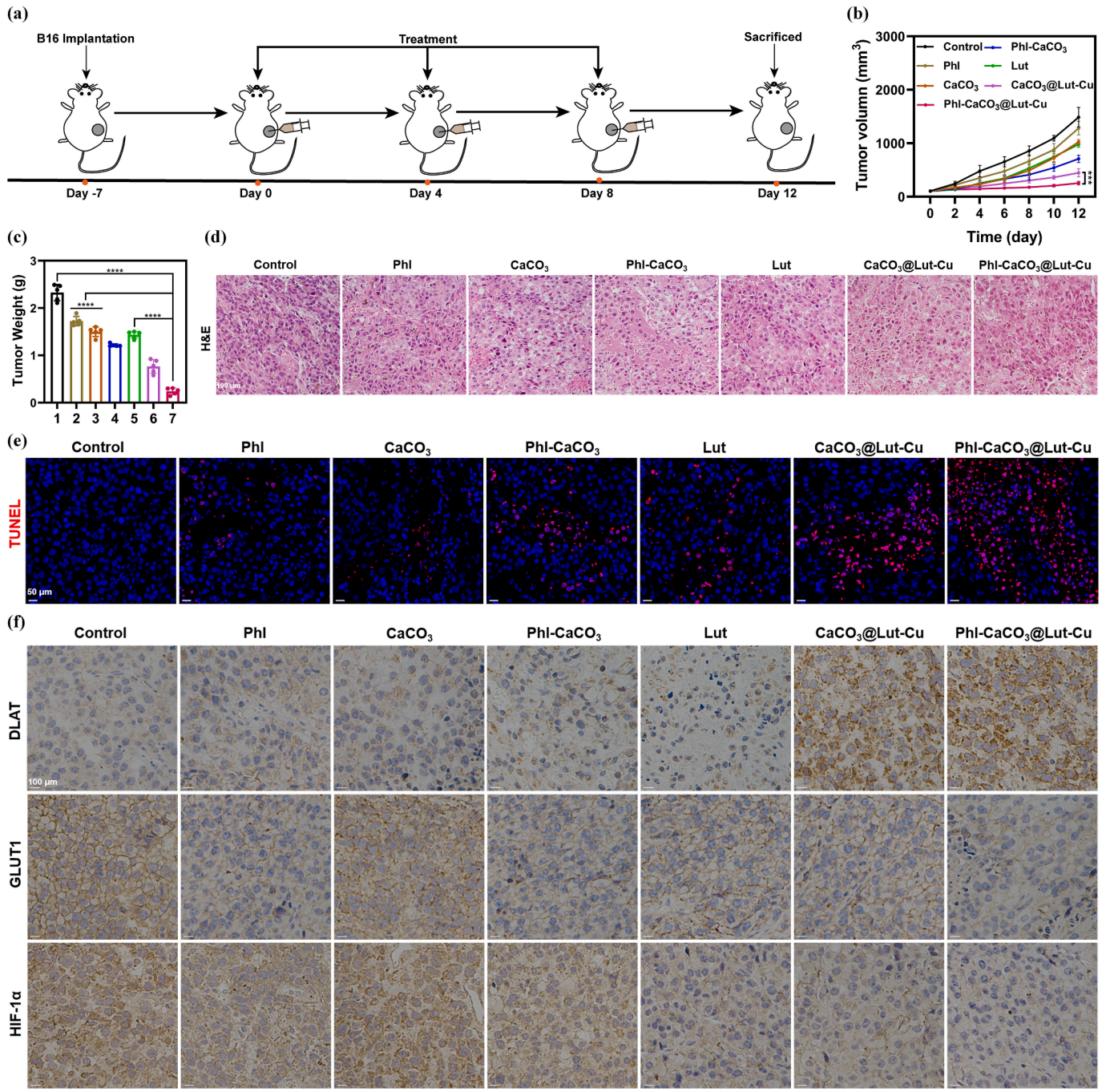

Fig. 5. In vivo antitumor efficacy of Phl-$CaCO_3$@Lut-Cu. (a) Schematic illustration of the experimental schedule for subcutaneous B16 tumor model treatment. The tumor volumn (b) and tumor weight (c) of mice after different treatments. (d) H&E staining of tumor sections after different treatments. (e) TUNEL immunofluorescence image of B16 tumor-bearing mice with various treatments. (f) DLAT, GLUT1, and HIF-1α immunohistochemical staining in tumor sections at the end of the treatment. (1:Control, 2:Phl, 3:$CaCO_3$, 4:Phl-$CaCO_3$, 5:Lut, 6:$CaCO_3$@Lut-Cu, 7:Phl-$CaCO_3$@Lut-Cu). (n = 5, $^{*}P < 0.05$, $^{**}P < 0.01$, $^{***}P < 0.001$, $^{****}P < 0.0001$).

times, indicating a convincing effect of cuproptosis in B16 cells. Additionally, we evaluated the expression of DLAT by immunofluorescence imaging. As illustrated in Fig. 4l, the presence of DLAT in the copper-containing groups was markedly increased, while the non-copper-containing groups displayed minimal red fluorescence in the cells following treatment. The expression levels of FDX1 and LIAS were also analyzed. Compared with the control, $CaCO_3$, and Phl-$CaCO_3$ groups, the FDX1 and LIAS protein levels in the $CaCO_3$@Lut-Cu and Phl-$CaCO_3$@Lut-Cu groups were significantly downregulated (Figs. 4k, S7e, and f). These findings suggest that Phl-$CaCO_3$@Lut-Cu nanoparticles significantly induce cuproptosis.

We also assessed mitochondrial damage related to cuproptosis and calcium ion imbalance using mitochondrial membrane potential detection and bio-TEM techniques. As shown in Fig. S9, the mitochondrial membrane potential in the calcium ion and copper-treated groups ($CaCO_3$, Phl-$CaCO_3$, $CaCO_3$@Lut-Cu, and Phl-$CaCO_3$@Lut-Cu) was not significantly reduced compared with the control group, indicating that the treatment did not cause substantial mitochondrial damage. Furthermore, there was no significant mitochondrial damage observed in the Phl-$CaCO_3$@Lut-Cu group when compared with the untreated control group (Fig. S10). The mitochondrial structure appeared relatively intact, with no noticeable loss of cristae. This may be attributed to

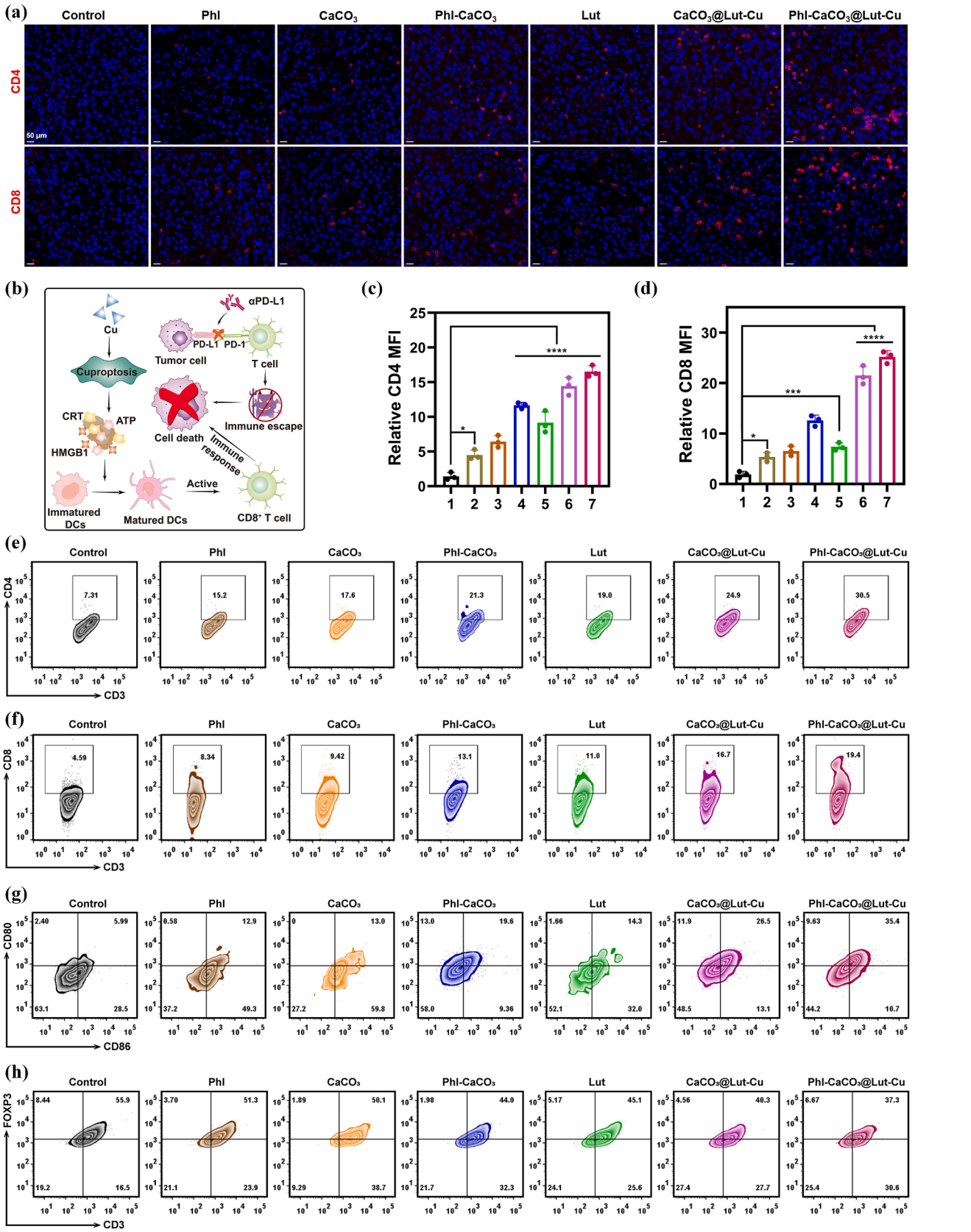

Fig. 6. Evaluation of in vivo antitumor immunity evoked by Phl-$CaCO_3$@Lut-Cu. (a) Immunofluorescence images of CD4 and CD8 in tumor sections. (b) Mechanism of immune response evoked by the combination of Phl-$CaCO_3$@Lut-Cu and αPD-L1. (c, d) The corresponding mean fluorescence intensity of CD4 and CD8. Representative flow cytometry plots of $CD4^+$ T cells (e), $CD8^+$ T cells (f), DCs maturation (g), and Treg cells (h) in tumors after various treatments. (1:Control, 2:Phl, 3:$CaCO_3$, 4:Phl-$CaCO_3$, 5:Lut, 6:$CaCO_3$@Lut-Cu, 7:Phl-$CaCO_3$@Lut-Cu).

the ability of both phloretin and luteolin to scavenge reactive oxygen species generated by Cu^{2+} redox reactions, thereby alleviating mitochondrial damage to some extent. In summary, the Phl-$CaCO_3$@Lut-Cu nanosystem does not induce significant damage to mitochondria.

3.5.3. Immunogenic cell death by cuproptosis

Cuproptosis induces immunogenic cell death (ICD) in dying tumor cells, which in turn releases DAMPs. Thus, the expression levels of HMGB1, CRT, and extracellular ATP were evaluated using immunofluorescence imaging and an ATP detection kit. Compared with the other treatments, cells treated with Phl-$CaCO_3$@Lut-Cu released more HMGB1 and exhibited the weakest red fluorescence signal (Fig. 4n). Similarly, the Phl-$CaCO_3$@Lut-Cu group exhibited the greatest CRT expression, and the strongest red fluorescence signal was clearly observed (Fig. S11). The extracellular ATP concentration data exhibited a comparable trend, with the Phl-$CaCO_3$@Lut-Cu group having the highest extracellular ATP concentration (Fig. 4m). In conclusion, these results suggest that Phl-$CaCO_3$@Lut-Cu activates the immune response by inducing release of DAMPs from tumor cells through cuproptosis.

3.6. In vivo antitumor activity of Phl-$CaCO_3$@Lut-Cu

To assess the *in vivo* biosafety of Phl-$CaCO_3$@Lut-Cu, we examined the pathology of major tissues and organs in C57BL/6 mice following subcutaneous administration of Phl-$CaCO_3$@Lut-Cu by H&E staining (Fig. S12). The results demonstrated that there were no significant pathological changes in the main organs and tissues of the mice, and there were no obvious abnormalities in the blood and biochemical indicator tests (Fig. S13). This suggested that Phl-$CaCO_3$@Lut-Cu exhibited high biological safety.

The B16 xenograft tumor model was then established in C57BL/6 mice and the administration scheme is shown in Fig. 5a. When the tumor volume reached 100 mm^3, intratumoral injections of different formulations were conducted and changes in mouse weight and tumor volume were recorded. As shown in Fig. S14, there was no significant change in mouse body weight, which further illustrated the biosafety of Phl-$CaCO_3$@Lut-Cu nanoparticles. In addition, Phl, $CaCO_3$, Phl-$CaCO_3$, Lut, $CaCO_3$@Lut-Cu, and Phl-$CaCO_3$@Lut-Cu all exhibited anti-tumor effects compared with the rapidly growing tumors in the control group (Figs. 5b and S15a). The Phl-$CaCO_3$@Lut-Cu treatment group exhibited the slowest tumor growth rate, and tumor volume was controlled at approximately 253.48 mm^3 at the end of the treatment cycle. The tumor weight was also the smallest in the Phl-$CaCO_3$@Lut-Cu group (Fig. 5c). These results suggest that the synergistic effects of dual glycolysis inhibition and cuproptosis efficiently suppress tumor growth and exhibit promising anti-tumor efficacy.

To further investigate changes during tumor proliferation, tumors were collected and then analyzed by H&E, Ki67, and TUNEL staining. As shown in Fig. 5d, the Phl-$CaCO_3$@Lut-Cu treatment group exhibited significant nuclear shrinkage, rupture, and nuclear lysis. Compared with the control group, the expression of Ki67 was significantly reduced, and the red fluorescence intensity in TUNEL staining was significantly increased (Figs. 5e and S15b), indicating remarkable enhancement of apoptosis and potent tumor growth inhibition by Phl-$CaCO_3$@Lut-Cu.

To further explore the anti-tumor mechanism of Phl-$CaCO_3$@Lut-Cu *in vivo*, the expression of DLAT, GLUT1, and HIF-1α were determined by immunohistochemistry (Figs. 5f and S16). There was significantly upregulated DLAT protein oligomerization in the groups containing copper, demonstrating the anti-tumor effect of cuproptosis in $CaCO_3$@Lut-Cu and Phl-$CaCO_3$@Lut-Cu groups *in vivo*. In addition, the expression levels of GLUT1 and HIF-1α reached their lowest points after Phl-$CaCO_3$@Lut-Cu treatment. This could be attributed to synergistic inhibition of GLUT1 by Phl and HIF-1α by Lut. These results collectively indicate that Phl-$CaCO_3$@Lut-Cu exerts a significant tumor therapeutic effect through dual inhibition of glycolysis.

3.7. Evaluation of antitumor immune effect of Phl-$CaCO_3$@Lut-Cu

Encouraged by the potent therapeutic effect of Phl-$CaCO_3$@Lut-Cu nanoparticles, we investigated their ability to activate the immune response (Figs. 6a, c, d, and S17). Compared with the control group, a significant increase in HMGB1 release and enhanced surface expression of CRT were observed after Phl-$CaCO_3$@Lut-Cu treatment. These findings were consistent with the *in vitro* results, indicating that cuproptosis can promote release of DAMPs, which in turn induce the immune response. In addition, in the CD4 and CD8 immunofluorescence experiment, the red fluorescence signal was significantly enhanced in the Phl-$CaCO_3$@Lut-Cu group, indicating that Phl-$CaCO_3$@Lut-Cu treatment could significantly increase CD4/CD8 infiltration and activate an immune response.

Flow cytometry was conducted to quantify immune cells (Figs. 6e–h and S18). Satisfyingly, the proportion of $CD4^+$ and $CD8^+$ T cells significantly increased following treatment with Phl-$CaCO_3$@Lut-Cu. Specifically, the frequency of $CD4^+$ T cells rose from 7.80 % to 29.82 %, representing increases of 2.10, 1.79, and 1.53 times compared with the Phl, $CaCO_3$, and Lut groups, respectively. Similarly, the proportion of $CD8^+$ T cells exhibited a comparable trend, reaching 20.48 % compared with 5.68 % in the control group (Figs. 6e, f, S18c and d). The frequency of mature DC cells was approximately 35.30 %, which was 4.47 times higher than that in the control group. However, the proportions of mature DCs in the Phl, $CaCO_3$, and Lut groups were only 10.95 %, 12.42 %, and 13.32 %, respectively (Figs. 6g and S18e). This confirmed that the interaction between Phl-$CaCO_3$@Lut-Cu and tumor cells triggered release of DAMPs from dying tumor cells, facilitating maturation of DC cells, enhancing activation of T cells, and ultimately inducing an immune response.

Studies have shown that tumor cells produce lactate and ATP after ingesting glucose for aerobic glycolysis. This is followed by efflux of lactate, inducing formation of a micro-acidic and tumor immunosuppressive microenvironment. Therefore, to further evaluate the reprogramming capability of Phl-$CaCO_3$@Lut-Cu in the tumor immunosuppressive microenvironment, we determined the frequencies of Treg and M1/M2 cells by flow cytometry (Fig. 6h, S18a, b, and f–h). Compared with the other groups, the number of Treg cells after Phl-$CaCO_3$@Lut-Cu treatment was significantly reduced from 55.30 % to 39.02 %, 0.70 times that of the control group (Figs. 6h and S18f). In addition, the number of M1 macrophages in the Phl-$CaCO_3$@Lut-Cu group was significantly increased by 26.72 %, which was 3.68 times higher than that of the control group (Fig. S18a and g). In contrast, the number of M2 macrophages was greatly reduced to 4.12 %, which was 0.14 times that of the control group (Fig. S18b and h). The results indicated that Phl-$CaCO_3$@Lut-Cu treatment induced polarization of macrophages from M2 to M1 type. This effect was mainly attributed to the ability of Phl and Lut to alter the macrophage phenotype and modify the tumor microenvironment by regulating glycolysis [46]. These results suggest that Phl-$CaCO_3$@Lut-Cu can potently reshape the tumor immunosuppressive microenvironment, thereby facilitating effective treatment of melanoma.

ELISA kits were used to detect the secretion of cytokines such as TNF-α, IL-6, IL-12p70, and IFN-γ, which play crucial roles in the immune response. As shown in Fig. S19, compared with the control group, the levels of the aforementioned cytokines were significantly upregulated after Phl-$CaCO_3$@Lut-Cu treatment. These results further illustrate that Phl-$CaCO_3$@Lut-Cu is able to effectively activate the immune response *in vivo* to kill tumor cells.

3.8. The antitumor efficacy of Phl-$CaCO_3$@Lut-Cu combined with αPD-L1

The immune checkpoint inhibitor αPD-L1 is a commonly used immunotherapeutic agent in the treatment of tumors. It blocks tumor cell immune evasion by binding to the PD-L1 receptor on the surface of

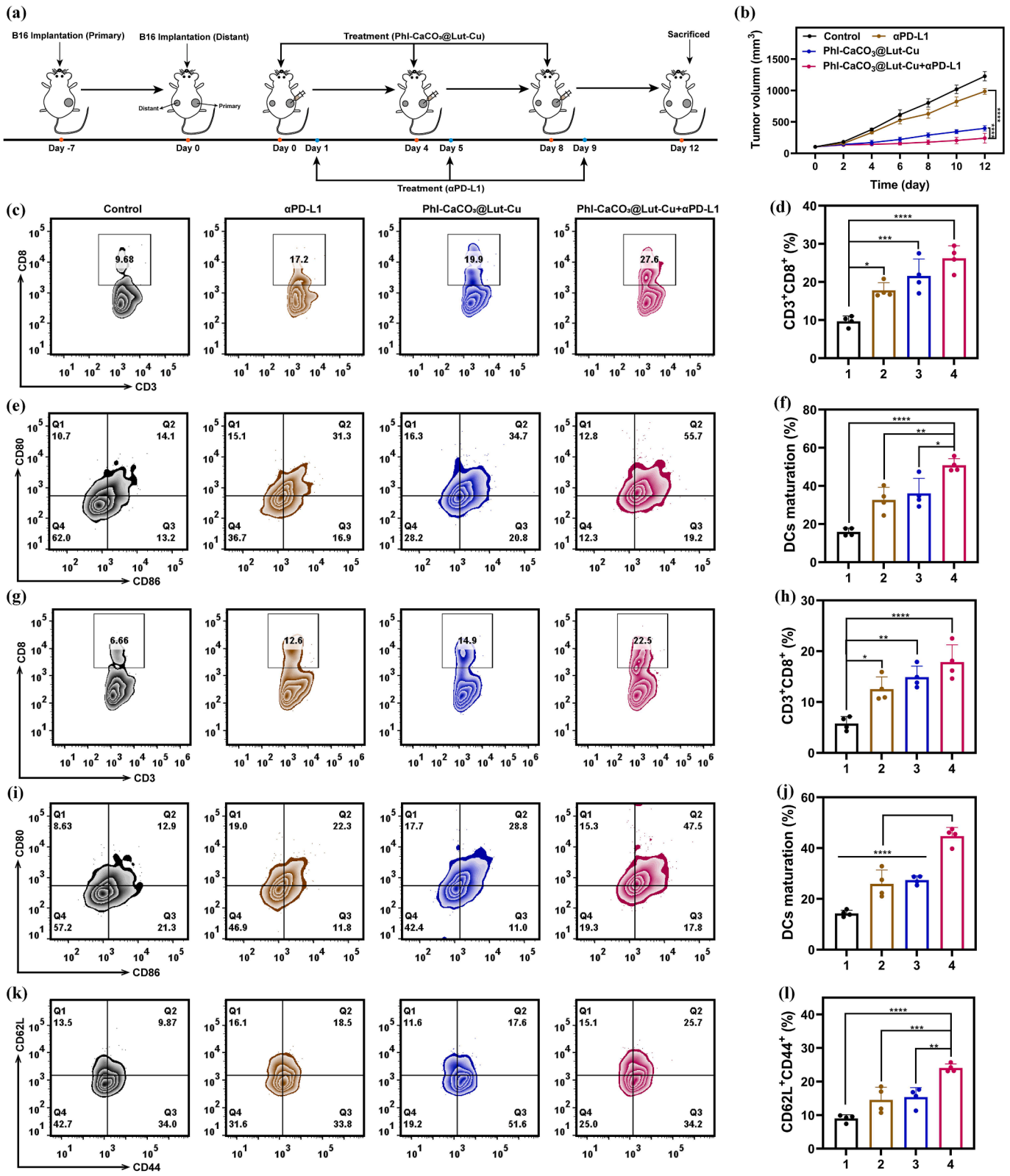

Fig. 7. Evaluation of antitumor efficacy of Phl-$CaCO_3$@Lut-Cu combined with αPD-L1 at B16 bilateral tumor models. (a) Schematic illustration of the experimental schedule for subcutaneous B16 bilateral tumor models. (b) The volumn of primary tumors. Representative flow cytometry plots and the corresponding quantitative analysis of $CD8^+$ T cells (c, d) and DCs maturation (e, f) of primary tumor. Representative flow cytometry plots and the corresponding quantitative analysis of $CD8^+$ T cells (g, h) and DCs maturation (i, j) of distal tumor. (k, l) Representative flow cytometry plots and the corresponding quantitative analysis of T_{cm} cells of spleen. (1: Control, 2:αPD-L1, 3:Phl-$CaCO_3$@Lut-Cu, 4:Phl-$CaCO_3$@Lut-Cu + αPD-L1). (n = 4, $^*P < 0.05$, $^{**}P < 0.01$, $^{***}P < 0.001$, $^{****}P < 0.0001$).

tumor cells, thereby restoring the ability of T cells to kill tumor cells. However, the effect of αPD-L1 has been reported to be limited by the immunosuppressive microenvironment when used as monotherapy, and ultimately its tumor-killing effect is weakened. In view of the ability of Phl-$CaCO_3$@Lut-Cu to reprogram the immunosuppressive microenvironment, we established a bilateral subcutaneous B16 tumor model in C57BL/6 mice to evaluate the effect of Phl-$CaCO_3$@Lut-Cu in combination with αPD-L1 (Fig. 7a).

The results showed that, compared with the control, αPD-L1, and Phl-$CaCO_3$@Lut-Cu groups, the Phl-$CaCO_3$@Lut-Cu + αPD-L1 combination treatment group exhibited the most effective inhibition of tumor growth. As shown in Figs. 7b and S20a, Phl-$CaCO_3$@Lut-Cu + αPD-L1 controlled the primary and distal tumor volumes to approximately 240.28 and 120.19 mm^3, respectively. Correspondingly, the Phl-$CaCO_3$@Lut-Cu + αPD-L1 combination treatment group also significantly reduced tumor weight. The primary tumor weights in the combination group were 0.07, 0.11, and 0.38 times those of the control, αPD-L1, and Phl-$CaCO_3$@Lut-Cu groups, respectively (Fig. S20c). The weights of the distal tumors exhibited the same trend (Fig. S20d). In addition, during the treatment period, there was no significant change in the body weight of mice treated with the different formulations (Fig. S20b), indicating good biocompatibility of the Phl-$CaCO_3$@Lut-Cu and αPD-L1 combination.

To further explore the capability of Phl-$CaCO_3$@Lut-Cu and αPD-L1 to remodel the immunosuppressive microenvironment, tumor tissues and spleens were collected from mice and immune cells were analyzed using flow cytometry (Figs. 7c–l and S21–S23). The proportions of $CD4^+$ (Fig. S21a and b) and $CD8^+$ T cells (Fig. 7c and d) in primary tumors from the Phl-$CaCO_3$@Lut-Cu + αPD-L1 group were 38.72 % and 26.20 %, and the proportions of $CD4^+$ (Fig. S22a and b) and $CD8^+$ T cells (Fig. 7g and h) in distal tumors were 22.00 % and 17.85 %, respectively. In comparison, the proportions of $CD4^+$ and $CD8^+$ T cells in primary tumors from the control group were only 7.95 % and 9.7 %, while the proportions of $CD4^+$ and $CD8^+$ T cells in distal tumors were 8.54 % and 5.8 %, respectively. The proportions of $CD4^+$ and $CD8^+$ T cells in primary tumors from the αPD-L1 monotherapy group were only 18.38 % and 17.8 %, while the proportions of $CD4^+$ and $CD8^+$ T cells in distal tumors were 14.45 % and 12.52 %, respectively. Furthermore, after treatment with Phl-$CaCO_3$@Lut-Cu + αPD-L1, the proportion of mature DC cells in primary and distal tumors increased from 15.92 % to 50.85 % and 14.28 % to 44.72 %, respectively (Fig. 7e, f, i, and j). The proportion of mature DCs in the primary tumor was 1.56 and 1.41 times higher than those observed in the αPD-L1 and Phl-$CaCO_3$@Lut-Cu treatment groups, respectively. We also measured the frequency of mature DCs in the lymph nodes using flow cytometry (Fig. S23). Compared with the control group, the Phl-$CaCO_3$@Lut-Cu + αPD-L1 treatment group increased the proportion of mature DCs from 8.56 % to 32.4 %, which was 1.51 and 1.13 times higher than those of the αPD-L1 and Phl-$CaCO_3$@Lut-Cu treatment groups, respectively. These results indicated that the Phl-$CaCO_3$@Lut-Cu + αPD-L1 combination effectively promoted maturation of DC cells, further enhancing the activation of T cells and inducing an immune response. The number of Treg cells was also determined. The proportions of Treg cells in primary tumors from the Phl-$CaCO_3$@Lut-Cu + αPD-L1 group were 0.71 and 0.75 times those from the αPD-L1 and Phl-$CaCO_3$@Lut-Cu groups, respectively (Fig. S21c and d). In the distal tumors, the proportions of Treg cells in the Phl-$CaCO_3$@Lut-Cu + αPD-L1 group were 0.70 and 0.73 times those in the αPD-L1 and Phl-$CaCO_3$@Lut-Cu groups, respectively (Fig. S22c and d). In addition, the proportion of T_{cm} in the Phl-$CaCO_3$@Lut-Cu + αPD-L1 treatment group increased from 9.01 % to 24.05 %. This represents an increase of 1.66 times compared with the αPD-L1 monotherapy group and 1.57 times that of the Phl-$CaCO_3$@Lut-Cu monotherapy treatment group (Fig. 7k and l), indicating its ability to effectively activate immune memory and exert long-term anti-tumor effects. Compared with other treatment groups, Phl-$CaCO_3$@Lut-Cu + αPD-L1 treatment increased the proportion of M1 macrophages in primary tumors from 17.05 % to 32.82 % (Fig. S21e and f), while decreasing the proportion of M2 macrophages from 40.60 % to 23.05 % (Fig. S21g and h). A comparable trend was observed in distal tumors (Fig. S22e, f, g, and h). In addition, upregulated secretion of TNF-α, IL-6, IL-12p70, and IFN-γ by tumors was detected using ELISA kits (Fig. S24), which indicated that Phl-$CaCO_3$@Lut-Cu combined with αPD-L1 was able to reshape the tumor microenvironment, activate the immune response, and induce long-term immune memory effects, which is conducive to enhanced therapeutic efficacy against tumors.

4. Conclusion

In this study, we developed Phl-$CaCO_3$@Lut-Cu nanoparticles that enhanced the efficacy of melanoma immunotherapy through synergistic dual inhibition of glycolysis and cuproptosis. Upon entry of Phl-$CaCO_3$@Lut-Cu into cells, phloretin, luteolin, and Cu^{2+} ions were released in response to the slightly acidic environment. Phloretin and luteolin inhibited glycolysis by blocking the activities of GLUT1 and HIF-1α, respectively. This reduced the production of intracellular glucose, lactate, and ATP, disrupting the energy supply of tumor cells and leading to downregulation of LDHA and ATP7B levels. Moreover, the overload of copper triggered oligomerization of DLAT protein and downregulated expression of Fe-S cluster proteins, FDX1 and LIAS, ultimately resulting in cuproptosis. Subsequently, cuproptosis prompted the release of DAMPs, upregulated expression of extracellular ATP, HMGB1, and CRT, and activated the immune response. Overall, the combination of Phl-$CaCO_3$@Lut-Cu and αPD-L1 exerted a powerful immunotherapeutic effect, which was manifested by promotion of DC maturation, increased infiltration of $CD4^+$ and $CD8^+$ T cells, decreased proportion of Treg cells, and transformation of M2 macrophages into M1 type. This study provides an important exploration of and valuable insights into the treatment of melanoma.

CRediT authorship contribution statement

Yanzhu Wang: Writing – original draft, Data curation. **Linghe Zang:** Methodology, Data curation. **Liyuan Guan:** Methodology, Investigation. **Xihang Ren:** Visualization, Methodology. **Zongmin Xia:** Software, Investigation. **Zhou Li:** Supervision. **Zhaoxu Meng:** Supervision, Project administration. **He Lian:** Writing – review & editing, Supervision, Project administration.

Declaration of competing interest

The authors declare that they have no known competing financial interests or personal relationships that could have appeared to influence the work reported in this paper.

Acknowledgments

This work was supported by the Scientific Research Projects of Liaoning Provincial Department of Education (Grant No: LJKMZ20221354, LJ212410163004), Natural Science Foundation of Liaoning Province (Grant No: 2023-MS-198), Cultivation Fund Project of National Natural Science Foundation (Grant No: PYJJ2021101) and Career Development Support Program for Young and Middle-aged Teachers (Grant No: ZQN202208) of Shenyang Pharmaceutical University. The authors would like to thank the Shiyanjia lab (www.Shiyanjia. com) for the TEM, XPS and thermogravimetric tests.

Appendix A. Supplementary data

Supplementary data to this article can be found online at https://doi.org/10.1016/j.cej.2024.158442.

Data availability

Data will be made available on request.

References

[1] A. Mastoraki, D. Schizas, V. Ntella, A. Roka, M. Vailas, I.S. Papanikolaou, P. Vassiliu, I. Papaconstantinou, Clinical evidence, diagnostic approach and challenging therapeutic modalities for malignant melanoma of the anorectum, ANZ J. Surg. 91 (3) (2021) 276–281, https://doi.org/10.1111/ans.16497.

[2] S. Adams, D.W. O'Neill, D. Nonaka, E. Hardin, L. Chiriboga, K. Siu, C.M. Cruz, A. Angiulli, F. Angiulli, E. Ritter, Immunization of malignant melanoma patients with full-length NY-ESO-1 protein using Toll-like receptor 7 agonist imiquimod as vaccine adjuvant, J. Immunol. 181 (1) (2008) 776, https://doi.org/10.4049/jimmunol.181.1.776.

[3] D.M. Pardoll, The blockade of immune checkpoints in cancer immunotherapy, Nat. Rev. Cancer 12 (4) (2012) 252–264, https://doi.org/10.1038/nrc3239.

[4] W. Zou, J.D. Wolchok, L. Chen, PD-L1 (B7–H1) and PD-1 pathway blockade for cancer therapy: mechanisms, response biomarkers, and combinations, Sci. Transl. Med. 8 (328) (2016) 3284, https://doi.org/10.1126/scitranslmed.aad7118.

[5] J.J. Luke, K.T. Flaherty, A. Ribas, G.V. Long, Targeted agents and immunotherapies: optimizing outcomes in melanoma, Nat. Rev. Clin. Oncol. 14 (8) (2017) 463–482, https://doi.org/10.1038/nrclinonc.2017.43.

[6] J. Afonso, L.L. Santos, A. Longatto-Filho, F. Baltazar, Competitive glucose metabolism as a target to boost bladder cancer immunotherapy, Nat. Rev. Urol. 17 (2) (2020) 77–106, https://doi.org/10.1038/s41585-019-0263-6.

[7] Y.C. Lee, H.M. Lam, C. Rosser, D. Theodorescu, W.C. Parks, K.S. Chan, The dynamic roles of the bladder tumour microenvironment, Nat. Rev. Urol. 19 (9) (2022) 515–533, https://doi.org/10.1038/s41585-022-00608-y.

[8] L. Zhang, Y. Wang, J. Karges, D. Tang, H. Zhang, K. Zou, J. Song, H. Xiao, Tetrahedral DNA nanostructure with interferon stimulatory DNA delivers highly potent toxins and activates the cGAS-STING pathway for robust chemotherapy and immunotherapy, Adv. Mater. 35 (8) (2023) 2210267, https://doi.org/10.1002/adma.202210267.

[9] L. Zhang, L. Zhu, L. Tang, J. Xie, Y. Gao, C. Yu, K. Shang, H. Han, C. Liu, Y. Lu, Glutathione-responsive nanoparticles of camptothecin prodrug for cancer therapy, Adv. Sci. 10 (3) (2023) 2205246, https://doi.org/10.1002/advs.202205246.

[10] Y. Cheng, C. Guo, S. Li, K. Deng, J. Tang, Q. Luo, S. Zhang, Y. Chang, T. Pan, Aquatic skin enabled by multi-modality iontronic sensing, Adv. Funct. Mater. 32 (18) (2022) e2205947.

[11] F. Voli, E. Valli, L. Lerra, K. Kimpton, F. Saletta, F.M. Giorgi, D. Mercatelli, J.R. C. Rouaen, S. Shen, J.E. Murray, A. Ahmed-Cox, G. Cirillo, C. Mayoh, P.A. Beavis, M. Haber, J.A. Trapani, M. Kavallaris, O. Vittorio, Intratumoral copper modulates PD-L1 expression and influences tumor immune evasion, Cancer Res. 80 (19) (2020) 4129–4144, https://doi.org/10.1158/0008-5472.CAN-20-0471.

[12] L. Xu, M. Peng, T. Gao, D. Wang, X. Lian, H. Sun, J. Shi, Y. Wang, P. Wang, Nanoenabled intracellular metal ion homeostasis regulation for tumor therapy, Adv. Sci. (Weinh.) 11 (7) (2024) e2306203.

[13] S. Kostka, M. Hosseini, Epple, In-Vitro Cell Response to Strontium/Magnesium-Doped Calcium Phosphate Nanoparticles, Micro. 3 (1) (2023) 156–171, https://doi.org/10.3390/micro3010012.

[14] L.M. Gaetke, H.S. Chow-Johnson, C.K. Chow, Copper: toxicological relevance and mechanisms, Arch. Toxicol. 88 (11) (2014) 1929–1938, https://doi.org/10.1007/s00204-014-1355-y.

[15] J. An, M. Liu, L. Zhao, W. Lu, S. Wu, K. Zhang, J. Liu, Z. Zhang, J. Shi, Boosting tumor immunotherapy by bioactive nanoparticles via Ca2+ interference mediated TME reprogramming and specific PD-L1 depletion, Adv. Funct. Mater. 32 (24) (2022) e2201275.

[16] X. Zhao, K. Zhang, Y. Wang, W. Jiang, H. Cheng, Q. Wang, T. Xiang, Z. Zhang, J. Liu, J. Shi, Intracellular self-assembly driven nucleus-targeted photo-immune stimulator with chromatin decompaction function for robust innate and adaptive antitumor immunity, Adv. Funct. Mater. 32 (17) (2022) e2108883.

[17] S. Wu, K. Zhang, Y. Liang, Y. Wei, J. An, Y. Wang, J. Yang, H. Zhang, Z. Zhang, J. Liu, J. Shi, Nano-enabled tumor systematic energy exhaustion via zinc (II) interference mediated glycolysis inhibition and specific GLUT1 depletion, Adv. Sci. (Weinh.) 9 (7) (2022) e2103534.

[18] Q. Cheng, X. Shi, Y. Chen, Q. Li, J. Wang, H. Li, L. Wang, Z. Wang, Tumor microenvironment-activatable nanosystem capable of overcoming multiple therapeutic obstacles for augmenting immuno/metal-ion therapy, ACS Nano 18 (12) (2024) 8996–9010, https://doi.org/10.1021/acsnano.3c12745.

[19] X. Zhao, H. Cheng, Q. Wang, W. Nie, Y. Yang, X. Yang, K. Zhang, J. Shi, J. Liu, Regulating photosensitizer metabolism with DNAzyme-loaded nanoparticles for amplified mitochondria-targeting photodynamic immunotherapy, ACS Nano 17 (14) (2023) 13746–13759, https://doi.org/10.1021/acsnano.3c03308.

[20] P. Tsvetkov, S. Coy, B. Petrova, M. Dreishpoon, A. Verma, M. Abdusamad, J. Rossen, L. Joesch-Cohen, R. Humeidi, R.D. Spangler, J.K. Eaton, E. Frenkel, M. Kocak, S.M. Corsello, S. Lutsenko, N. Kanarek, S. Santagata, T.R. Golub, Copper induces cell death by targeting lipoylated TCA cycle proteins, Science 375 (6586) (2022) 1254–1261, https://doi.org/10.1126/science.abf0529.

[21] X.-K. Jin, J.-L. Liang, S.-M. Zhang, Q.-X. Huang, S.-K. Zhang, C.-J. Liu, X.-Z. Zhang, Orchestrated copper-based nanoreactor for remodeling tumor microenvironment to amplify cuproptosis-mediated anti-tumor immunity in colorectal cancer, Mater. Today 68 (2023) 108–124, https://doi.org/10.1016/j.mattod.2023.06.024.

[22] M.V. Liberti, J.W. Locasale, The Warburg effect: how does it benefit cancer cells, Trends Biochem. Sci 41 (3) (2016) 211–218, https://doi.org/10.1016/j.tibs.2015.12.001.

[23] Y.P. Wang, W. Zhou, J. Wang, X. Huang, Y. Zuo, T.S. Wang, X. Gao, Y.Y. Xu, S. W. Zou, Y.B. Liu, J.K. Cheng, Q.Y. Lei, Arginine Methylation of MDH1 by CARM1 inhibits glutamine metabolism and suppresses pancreatic cancer, Mol. Cell 64 (4) (2016) 673–687, https://doi.org/10.1016/j.molcel.2016.09.028.

[24] L. Li, Y. Liang, L. Kang, Y. Liu, S. Gao, S. Chen, Y. Li, W. You, Q. Dong, T. Hong, Z. Yan, S. Jin, T. Wang, W. Zhao, H. Mai, J. Huang, X. Han, Q. Ji, Q. Song, C. Yang, S. Zhao, X. Xu, Q. Ye, Transcriptional regulation of the warburg effect in cancer by SIX1, Cancer, Cell. 33 (3) (2018) 368–385 e7, doi: 10.1016/j.ccell.2018.01.010.

[25] H.L. Caslin, D. Abebayehu, J.A. Pinette, J.J. Ryan, Lactate is a metabolic mediator that shapes immune cell fate and function, Front. Physiol. 12 (2021) 688485, https://doi.org/10.3389/fphys.2021.688485.

[26] M.J. Watson, P.D.A. Vignali, S.J. Mullett, A.E. Overacre-Delgoffe, R.M. Peralta, S. Grebinoski, A.V. Menk, N.L. Rittenhouse, K. DePeaux, R.D. Whetstone, D.A. A. Vignali, T.W. Hand, A.C. Poholek, B.M. Morrison, J.D. Rothstein, S.G. Wendell, G.M. Delgoffe, Metabolic support of tumour-infiltrating regulatory T cells by lactic acid, Nature 591 (7851) (2021) 645–651, https://doi.org/10.1038/s41586-020-03045-2.

[27] J.T. Noe, B.E. Rendon, A.E. Geller, L.R. Conroy, S.M. Morrissey, L.E.A. Young, R. C. Bruntz, E.J. Kim, A. Wise-Mitchell, M.B.D.S. Rizzo, Lactate supports a metabolic-epigenetic link in macrophage polarization, Sci. Adv. 7 (46) (2021) eabi8602, https://doi.org/10.1126/sciadv.abi8602.

[28] H. Kanemaru, Y. Mizukami, A. Kaneko, H. Tagawa, T. Kimura, H. Kuriyama, S. Sawamura, I. Kajihara, K. Makino, A. Miyashita, J. Aoi, T. Makino, S. Masuguchi, S. Fukushima, H. Ihn, A mechanism of cooling hot tumors: lactate attenuates inflammation in dendritic cells, iScience. 24 (9) (2021) 103067, https://doi.org/10.1016/j.isci.2021.103067.

[29] A. Brand, K. Singer, G.E. Koehl, M. Kolitzus, G. Schoenhammer, A. Thiel, C. Matos, C. Bruss, S. Klobuch, K. Peter, M. Kastenberger, C. Bogdan, U. Schleicher, A. Mackensen, E. Ullrich, S. Fichtner-Feigl, R. Kesselring, M. Mack, U. Ritter, M. Schmid, C. Blank, K. Dettmer, P.J. Oefner, P. Hoffmann, S. Walenta, E. K. Geissler, J. Pouyssegur, A. Villunger, A. Steven, B. Seliger, S. Schreml, S. Haferkamp, E. Kohl, S. Karrer, M. Berneburg, W. Herr, W. Mueller-Klieser, K. Renner, M. Kreutz, LDHA-associated lactic acid production blunts tumor immunosurveillance by T and NK cells, Cell Metab. 24 (5) (2016) 657–671, https://doi.org/10.1016/j.cmet.2016.08.011.

[30] B.Y. Choi, Biochemical basis of anti-cancer-effects of Phloretin-A natural dihydrochalcone, Molecules 24 (2) (2019) 278, https://doi.org/10.3390/molecules24020278.

[31] A. Takeno, I. Kanazawa, K.I. Tanaka, M. Notsu, T. Sugimoto, Phloretin suppresses bone morphogenetic protein-2-induced osteoblastogenesis and mineralization via inhibition of phosphatidylinositol 3-kinases/Akt pathway, Int. J. Mol. Sci. 20 (10) (2019), https://doi.org/10.3390/ijms20102481.

[32] S.J. Cho, J.S. Moon, C.M. Lee, A.M. Choi, H.W. Stout-Delgado, Glucose transporter 1-dependent glycolysis is increased during aging-related lung fibrosis, and phloretin inhibits lung fibrosis, Am. J. Respir. Cell Mol. Biol. 56 (4) (2017) 521–531, https://doi.org/10.1165/rcmb.2016-0225OC.

[33] L.L. Miguel, Distribution and biological activities of the flavonoid luteolin, MRMC 9 (1) (2009) 31–59, https://doi.org/10.2174/138955709787001712.

[34] Y. Li, L. Shen, H. Luo, Luteolin ameliorates dextran sulfate sodium-induced colitis in mice possibly through activation of the Nrf2 signaling pathway, Int. Immunopharmacol. 40 (2016) 24–31, https://doi.org/10.1016/j.intimp.2016.08.020.

[35] C. Li, Q. Wang, S. Shen, X. Wei, G. Li, HIF-1α/VEGF signaling-mediated epithelial-mesenchymal transition and angiogenesis is critically involved in anti-metastasis effect of luteolin in melanoma cells, Phytother. Res. 33 (3) (2019) 798–807, https://doi.org/10.1002/ptr.6273.

[36] G. Gabriely, M.A. Wheeler, M.C. Takenaka, F.J. Quintana, Role of AHR and HIF-1α in glioblastoma metabolism, Trends Endocrinol. Metab. 28 (6) (2017) 428–436, https://doi.org/10.1016/j.tem.2017.02.009.

[37] Z. Dong, L. Feng, Y. Hao, M. Chen, M. Gao, Y. Chao, H. Zhao, W. Zhu, J. Liu, C. Liang, Q. Zhang, Z. Liu, Synthesis of hollow biomineralized CaCO(3)-polydopamine nanoparticles for multimodal imaging-guided cancer photodynamic therapy with reduced skin photosensitivity, J. Am. Chem. Soc. 140 (6) (2018) 2165–2178, https://doi.org/10.1021/jacs.7b11036.

[38] J. Chen, J. Li, J. Zhou, Z. Lin, F. Cavalieri, E. Czuba-Wojnilowicz, Y. Hu, A. Glab, Y. Ju, J.J. Richardson, F. Caruso, Metal-phenolic coatings as a platform to trigger endosomal escape of nanoparticles, ACS Nano 13 (10) (2019) 11653–11664, https://doi.org/10.1021/acsnano.9b05521.

[39] Y. Liu, C. Fan, L. Pu, C. Wei, H. Jin, Y. Teng, M. Zhao, A.C. Yu, F. Jiang, J. Shu, F. Li, Q. Peng, J. Kong, B. Pan, L. Zheng, Y. Huang, Phloretin induces cell cycle arrest and apoptosis of human glioblastoma cells through the generation of reactive oxygen species, J. Neurooncol 128 (2) (2016) 217–223, https://doi.org/10.1007/s11060-016-2107-z.

[40] Z. Chen, B. Zhang, F. Gao, R. Shi, Modulation of G(2)/M cell cycle arrest and apoptosis by luteolin in human colon cancer cells and xenografts, Oncol. Lett. 15 (2) (2018) 1559–1565, https://doi.org/10.3892/ol.2017.7475.

[41] C. He, J. Wang, T. Chakraborty, S. Roy, A newfangled coordinated ruthenium phloretin complex reprogramming breast cancer microenvironment interceded by modulation of PI3K/Akt/Mtor/VEGF pathway and modifying the antioxidant status correlated with intensified apoptotic events, Res. Sq. 1–29 (2020), https://doi.org/10.21203/rs.3.rs-42460/v1.

[42] H.W. Leung, C.H. Wu, C.H. Lin, H.Z. Lee, Luteolin induced DNA damage leading to human lung squamous carcinoma CH27 cell apoptosis, Eur. J. Pharmacol. 508 (1–3) (2005) 77–83, https://doi.org/10.1016/j.ejphar.2004.12.032.
[43] J.L. Sagripanti, P.L. Goering, A. Lamanna, Interaction of copper with DNA and antagonism by other metals, Toxicol. Appl. Pharmacol. 110 (3) (1991) 477–485, https://doi.org/10.1016/0041-008X(91)90048-J.
[44] C. Zimmer, G. Luck, H. Fritzsche, H. Triebel, DNA–copper(II) complex and the DNA conformation, Biopolymers 10 (3) (1971) 441–463, https://doi.org/10.1002/bip.360100303.
[45] J. Yao, S. Man, H. Dong, L. Yang, L. Ma, W. Gao, Combinatorial treatment of Rhizoma Paridis saponins and sorafenib overcomes the intolerance of sorafenib, J. Steroid Biochem. Mol. Biol. 183 (2018) 159–166, https://doi.org/10.1016/j.jsbmb.2018.06.010.
[46] O.R. Colegio, N.Q. Chu, A.L. Szabo, T. Chu, A.M. Rhebergen, V. Jairam, N. Cyrus, C.E. Brokowski, S.C. Eisenbarth, G.M. Phillips, G.W. Cline, A.J. Phillips, R. Medzhitov, Functional polarization of tumour-associated macrophages by tumour-derived lactic acid, Nature 513 (7519) (2014) 559–563, https://doi.org/10.1038/nature13490.